Search for Gamma-Rays from the Annihilation of Supersymmetric Dark Matter with H.E.S.S.

Diplomarbeit

von

Constanze Jahn

Erlangen Centre for Astroparticle Physics
Physikalisches Institut
Lehrstuhl für Teilchen- und Astroteilchenphysik
Friedrich-Alexander-Universität
Erlangen-Nürnberg

1. Gutachter: Prof. Dr. G. Anton
2. Gutachter: Prof. Dr. C. Stegmann

6. November 2008

Abstract

The High Energy Stereoscopic System (H.E.S.S.) consists of four Imaging Atmospheric Cherenkov Telescopes. With an energy threshold of about 100 GeV the system is suitable for the search for supersymmetric dark matter. Theories predict, that Supersymmetric dark matter annihilates in the galactic halo and thereby produces gamma-rays, which propagate to the earth.
The aim of this work is to study the detection of gamma-rays originating from dark matter annihilation with H.E.S.S.. Therefore the expected gamma-ray signal from supersymmetric dark matter annihilation is studied more closely. The program tool DarkSUSY5.0.1 is used for the calculates of the properties of the supersymmetric dark matter. In addition the derivation of an upper limit on the velocity weighted annihilation cross section of different supersymmetric models is given. The work closes with the introduction of a new approach in the detection of dark matter with H.E.S.S.. This method is then applied on real data to test it.

Kurzfassung

Das Hochenergetische Stereoskopische System (H.E.S.S.) besteht aus vier abbildenden Cherenkov Teleskopen. Mit einer Energieschwelle von ungefähr 100 GeV ist das System zur Suche nach supersymmetrischer dunkler Materie geeignet. Theorien sagen vorraus, dass supersymmetrische dunkle Materie im galaktischen Halo annihiliert und dabei Gammastrahlen produziert, die zur Erde propagieren.
Das Ziel dieser Arbeit ist es zu untersuchen, ob mit H.E.S.S. Gammastrahlen, die aus der Annihilation von dunkler Materie stammen, detektiert werden können. Deswegen wird das erwartete Signal an Gammastrahlen aus der Annihilation supersymmetrischer dunkler Materie genauer untersucht. Das Programm Paket DarkSUSY5.0.1 wird für die Berechnung der Eigenschaften der supersymmetrischen dunklen Materie verwendet. Des Weiteren wird die Herleitung einer oberen Grenze an den mit der Geschwindigkeit gewichteten Wirkungsquerschnitt verschiedener supersymmetrischer Modelle angegeben. Die Arbeit endet mit der Einführung einer neuen Herangehensweise an die Detektion dunkler Materie mit H.E.S.S.. Diese Methode wird dann auf echte Daten angewendet um sie zu testen.

Contents

1 Introduction

The universe is rich in bright stars and glowing gases. At least it seems like that looking at skymaps such as Hubble deep field (Fig. 1.1). But a closer look uncovers that the universe is not bright at all. The universe is mostly dark. Most of the matter in the universe is unseen by humans. Nevertheless physicists reveal more and more about this mysterious dark part of the universe. This 'invisible' matter is called dark matter. Dark matter does not interact electromagnetically. It only interacts through gravitation. Today the quest for dark matter is one of the most important quests in astroparticle and particle physics. But the quest for dark matter is also one of the most difficult quests. How can something 'invisible' be seen? The answer to this question lies already in a statement made above. Dark matter is seen by gravitation and gravitational effects can be used to search for it. Furthermore dark matter still is 'ordinary' matter and therefore can scatter of matter particles. This enables a further way to search for dark matter. Finally particles, which do interact electromagnetically, can be produced from dark matter particles. These produced particles can then be detected with 'standard' detectors (meaning detectors, which use electromagnetic interactions to detect particles).

Such a standard detector is the High Energy Stereoscopic System (H.E.S.S.). It is an area of four Imaging Atmospheric Cherenkov Telescopes (IACTs). At the moment H.E.S.S. is the most sensitive ground based IACT. It has an energy threshold of about 100 GeV. Already H.E.S.S. has successfully detected many gamma-ray sources, e.g. supernova remnants, pulsar wind nebulae and active galactic nuclei (AGN), which do not originate from dark matter. But the origin of some sources is unknown, e.g. for the source HESS J1745-290 at the galactic centre. Such sources with unknown origin could be due to dark matter. This is tested, e.g. see [1]. Furthermore upper limits on the dark matter properties can be derived, e.g. [2].

The aim of this thesis is to get familiar with the basics of the search for supersymmetric dark matter with H.E.S.S.. In order to achieve this, an understanding of supersymmetric dark matter and of the H.E.S.S. analysis has to be gained. The program package DarkSUSY ([3]) is used to numerically calculate some of the properties of supersymmetric dark matter. In addition a new analysis in the search for dark matter is tested.

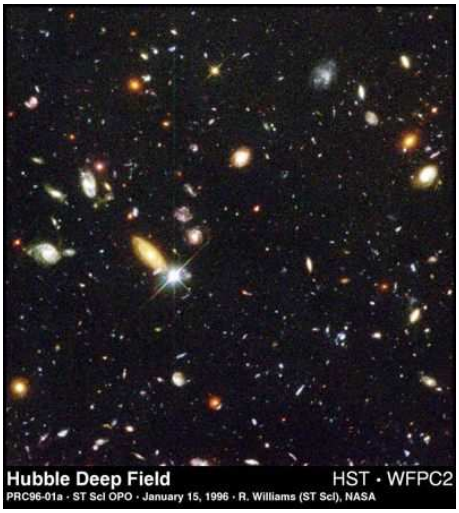

Figure 1.1: Shown is the Hubble deep field.

In the following dark matter is discussed in more details. Some evidence for dark matter is mentioned. Then a detailed description about Supersymmetry and especially supersymmetric dark matter follows. The properties of the dark matter important for the detection of it with gamma-rays are pointed out. Next a section follows introducing the H.E.S.S. experiment and its analysis methods, which have been used in this thesis. Eventually the work done in this thesis is presented. Several approaches have been taken in the study of the search for dark matter with the H.E.S.S. telescope. In the end a conclusion is given and further activities and possibilities in the dark matter search with H.E.S.S. are mentioned.

2 Dark Matter, Big Bang Cosmology and Experiments

The existence of dark matter is widely accepted. There are several evidence for the existence of dark matter. Dark matter already turns up when the origin of the universe is described by the Big Bang theory or Big Bang model of cosmology (Big Bang model) [6]. The Big Bang model is a theory describing the origin of the universe. This theory relies on two very basic principles. One is general relativity and the other one the Cosmological Principle. Both these principles are essentially theories, that are assumed to hold.
General relativity, which was introduced by Albert Einstein in 1915 [5], describes the relation between the geometry of spacetime and the gravitational interactions in that space. This relation is given by the Einstein's field equations (Eq.2.1).

$$R_{\mu\nu} - \frac{1}{2} g_{\mu\nu} R + g_{\mu\nu}\Lambda = \frac{8\pi G}{c^4} T_{\mu\nu} \tag{2.1}$$

There $g_{\mu\nu}$ is the metric tensor. $R_{\mu\nu}$ is the Ricci curvature tensor and R the scalar curvature. Λ is the cosmological constant, G the gravitational constant and $T_{\mu\nu}$ the stress-energy tensor. This states, that the shape of spacetime is connected to matter and energy in this spacetime. Today many experiments exist, that take precision measurements to test general relativity [4]. So far no contradiction between theory and experiment has been found. Hence general relativity is assumed to hold everywhere in our universe in the Big Bang theory.
The other pillar, on which the Big Bang model rests, is the Comological Principle. It states that on large scales the universe is homogeneous and isotropic. Again there exist measurements that justify this assumption. One is the measurement of the microwave background radiation done with WMAP satellite [6]. The microwave background radiation, which is supposed to be a left over from the Big Bang, has the same temperature over the whole universe. The temperature is only fluctuating at the level of mK (after the dipole anisotropy, that is due to the motion of the sun, has been subtracted). This can be seen in Fig. 2.1, where the measurement of the temperature of the cosmic microwavebackground radiation is shown at different scales. On top the isotropic and homogeneous distribution at large scales is shown, while at the bottom small changes at the order mK are visible. The observation of

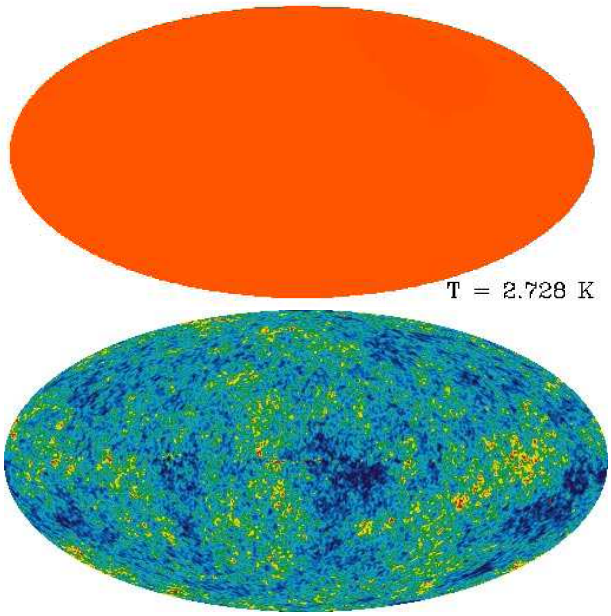

Figure 2.1: Shown is the temperature of the microwavebackground measured by WMAP [6]. On top at a scale of several Kelvin. Below the scale is much smaller and also little fluctuations in the temperature are visible.

galaxies and their redshift reveals that the universe is expanding. This evolution of the universe is described by the Friedmann equation (Eq. 2.2). These equation is derived from the Einstein's field equations.

$$H^2 \equiv \left(\frac{\dot{R}}{R}\right)^2 = \frac{8\pi G}{3}\rho_M + \frac{\Lambda}{3} - \frac{k}{R^2} \tag{2.2}$$

In Eq.2.2 $c = 1$. H is the Hubble parameter, which describes the rate of the expansion of the universe. This can also be expressed in terms of the scale factor $R(t)$. G is the gravitational constant and ρ_M the matter density. Λ is the cosmological constant, which is connected to the energy of the vacuum. Eventually k leads to a curvature of space-time. This equation can also be expressed in terms of the density parameters Ω. The density parameter Ω is defined as the ratio between the actual (measureable) density of all matter and energy in the universe and the critical density ρ_c. The critical density ρ_c is derived from the Friedmann equation by setting Λ ($\Lambda = 0$ yields $k = R^2(\frac{8\pi G}{3}\rho - H^2)$) and k equal to zero. This yields

$\rho_c = \frac{3H^2}{8\pi G}$. Now in terms of the matter density parameter Ω_M, the density parameter for the cosmological constant Ω_Λ and the density parameter for the curvature Ω_k the Friedmann equation looks like the following:

$$1 = \Omega_M + \Omega_\Lambda + \Omega_k \tag{2.3}$$

From Eq. 2.3 basic features of the universe can be derived. Especially in terms of the curvature and therefore the shape of the universe. Subtracting Ω_k in Eq. 2.3 results in the following: $1 - \Omega_k = \Omega_M + \Omega_\Lambda$. Now if $\Omega_k = 0$ the universe is flat, if $\Omega_k > 0$ it is closed and if $\Omega_k < 0$ it is open. This is also illustrated in Fig. 2.2. There the shapes for positive, negative and zero curvatures of space are shown.

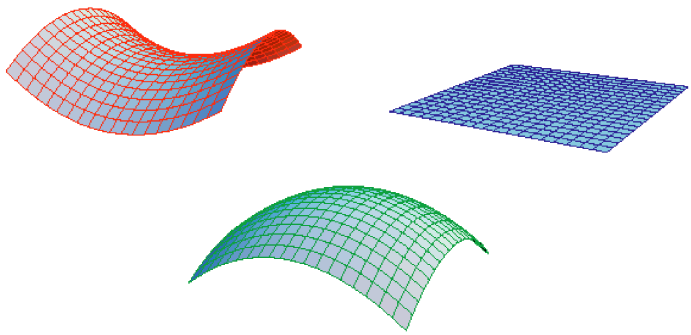

Figure 2.2: The shape of an open ($\Omega_k < 0$, on top left), a flat ($\Omega_k = 0$, on top right) and closed ($\Omega_k > 0$, below) universe are shown. The shapes are according to a negative curvature, a zero curvature or a positive curvature.

The question for the curvature of the universe is about to be answered as different measurement exclude more and more regions of the density parameters [8]. This exclusion limits are shown in Fig. 2.3. Exclusion regions on Ω_M and Ω_Λ from different experiments are plotted. From these exclusions a value for Ω_k of the order of 10^{-2} can be derived. This points towards a flat universe. The question for the composition of matter or energy in the universe arises. The values for the density parameters Ω_M and Ω_Λ can be determined to a certain degree. Ω_Λ is needed to explain for the acceleration of the universe. This energy, that accelerates the universe, is referred to as dark energy. It is introduced to reason for the observed fact that the universe is expanding ever faster. Though the question of the nature of dark energy is one of the greatest mysteries nowadays, it is impossible to fully answer it. No measurements can be made to determine the properties of dark energy. Therefore the matter density Ω_M, is studied in more detail in the following. The matter density Ω_M is of the amount of about 25%. The simplest assumption

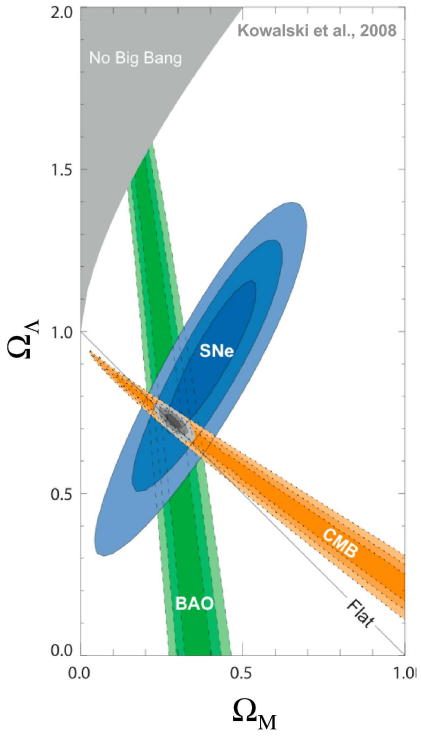

Figure 2.3: The exclusion limits on Ω_M and Ω_Λ as derived from different experiments. CMB are cosmic microwave background measurements. SNe are results from Supernovae measurements and BAO are baryon acoustic oscillations [8].

would be that the matter density is made up by the matter of stars and planets. But as a matter of fact it turns out, that the material seen by detectors such as telescopes etc. only account for about 1.25% of Ω_M [6]. This is shown in Fig. 2.4, where the composition of the universe measured by WMAP is shown. According to this, there must be more matter in the universe, which is not interacting electromagnetically. This matter is then called dark matter. This dark matter is essential to explain structure formation in the early universe. Fluctuations in the density of the dark matter yielded to clumping in the early universe and therefore to the formation of galaxies. But nevertheless is the Big Bang model only a theory. A theory, that fits quite nicely with today's experiments and measurements. Still such a theory alone would hardly be called evidence for dark matter. But the Big Bang model is one argument for the existence of dark matter.

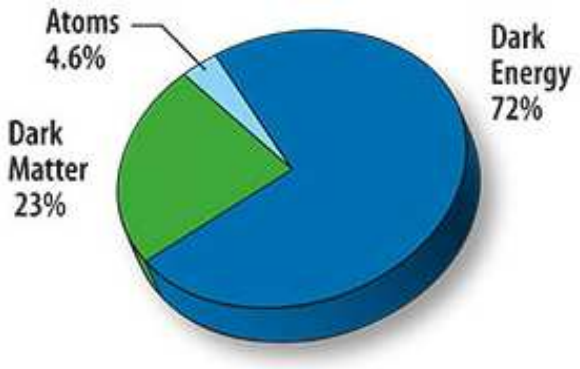

Figure 2.4: The composition of the universe as derived from WMAP data in 2008 [6].

As mentioned at the beginning of this section there are several evidences for dark matter. So in the following the historic path leading to experimental evidences for dark matter is described. In 1933 Fritz Zwicky was the first one, who observed indirectly dark matter. The Swiss astronomer worked at Caltech in the US, when he studied the Coma cluster of galaxies in detail [9]. Zwicky applied two different methods to derive the mass of the cluster. In the first method the luminosity of the cluster is used to derive the mass. The luminosity of the galaxies and stars within the cluster is measured and Zwicky estimated the mass of the Coma cluster with these measurements. The Viral theorem is the basis for the second method of mass derivation. From the Virial theorem a connection between the mass of the cluster and the velocity is known. From observations of the cluster Zwicky could calculate the velocities of the galaxies therein. Then he applied the Virial theorem and derived the mass of the cluster. He compared the two masses. The mass he derived from the luminosities to the mass, that he gained from the application of the Virial theorem on the measured velocity. To his great surprise he discovered a difference, that is at least of the order of one magnitude. The mass, that resulted from the use of the Virial theorem, is larger than that derived from the luminosity. An explanation for this contradiction is, that there is more matter in the cluster than that emitting radiation. This is the first hint of dark matter. But even though Zwicky's results were quite interesting, it was not until the late 1960s that they were studied more closely. At that time Vera Rubin, a young astronomer, made another discovery. She measured rotation curves of galaxies. A rotation curve in this context is the velocity distribution of stars depending on their distance to the centre of the galaxy. Taking Newton's law of gravity the rotation speed of stars in a spiral galaxy is expected to fall of at the edges of the galaxy. Rubin used a spectrometer to determine the redshift of the stars and hence their velocity. The

curves she measured all showed the same feature, mainly that the speed of the stars is roughly the same over the whole galaxy. This is sketched in Fig. 2.5. There the expected rotation curve and a rotation curve, that resembles the measured rotation curves, are shown.

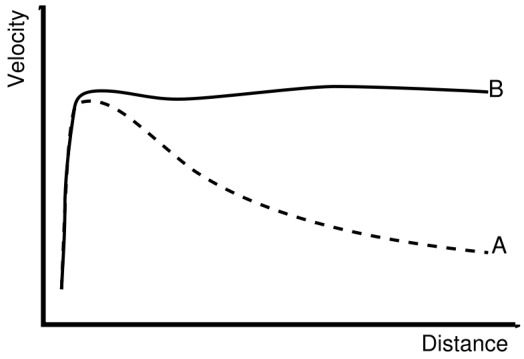

Figure 2.5: Sketch of how the galaxy rotation curves Rubin measured looked like. The dashed line corresponds to the expected curve A, while the solid line resembles the measurements B.

For Rubin's measurement in principle two explanations are possible. One is stating that Newtonian gravity doesn't hold throughout the whole universe. Therefore the law of gravitation has to be changed. But this explanation is not favoured, due to the fact that it violates the equivalence principle. The second theory though promotes the existence of additional matter. As in Zwicky's case, this matter then has to be dark matter, which does not radiate. Today the methods to derive the mass of the radiating parts of galaxies and cluster have improved. The mass can be derived from X-ray emissions to a higher precision [10]. A further method is gravitational lensing [11]. There it is assumed, that strong gravitational fields work like lenses on the light emitted by a very bright object. This gravitational fields are due to massive objects. Hence from the effect of the lensing the mass of the object can be determined. As the lensing is only due to gravitational interaction also dark matter can be seen with it, if it is massive enough. These experiments measure a mass-to-light ratio of about 10 to 1. So today the existence of dark matter is commonly accepted.

Many experiments search for dark matter. The search for dark matter can be direct or indirect. Some of the experiments, which search for dark matter directly, are listed in Tab. 2.1. They are all based on the same principle. They try to measure the recoil energy from a dark matter particle scattering of a nucleus. Due to the very low rate, at which this scattering happens, the background needs to be well

understood. In order to reduce the background from radioactivity and cosmic rays, these experiments are located underground, often in tunnels or mines. The recoil energy is measured in from of a little rise in temperature and/or a charge signal (ionisation) or a light signal (scintillation). Due to the different techniques the target masses needed by the experiments are different, see Tab. 2.1. Until now only limits are derived from the experiments and no detection of a dark matter particle (though a signal, which is measured by the DAMA collaboration, still needs to be fully understood).

Experiment	Location	Target	Mass [kg]
DAMA	Gran Sasso, Italy	Sodium iodide	100
CDMS II	Soudan, Minn., US	Silicon, germanium	7
CRESST II	Gran Sasso, Italy	Calcium tungsten oxide	10
EDELWEISS	Frejus, France	Germanium	1.3

Table 2.1: Different experiments, which directly search for dark matter.

The experiments, which search indirectly for dark matter, produce limits as well. These experiments are mostly telescopes searching for neutrinos or gamma-rays from the annihilation of dark matter. The search for neutrinos is done with neutrino telescopes, such as ICECUBE or ANTARES. The search for gamma-rays is done with a lot of different experiments, for the different energy ranges. Some of these experiments are located on satellites, e.g. EGRET, PAMELA and now FERMI (former GLAST). They usually take data in the low energy range up to a few TeV. From a few hundred GeV up to several TeV ground based imaging atmospheric cherenkov telescopes are used. Examples for such telescopes are MAGIC on the Canary Islands, CANGAROO in Australia and H.E.S.S. in Namibia.

There are different kinds of dark matter. Dark matter is divided into Hot Dark Matter (HDM), Warm Dark Matter (WDM) and Cold Dark Matter (CDM). HDM is ultrarelativistic, which means it is moving almost with the speed of light. WDM is relativistic and CDM moves non-relativistically. Examples for HDM are neutrinos, but they do not have enough mass to make up for the missing mass in the universe. Also they would not lead to clumping in the early universe. Sterile neutrinos are an example for WDM. But actually CDM is required, if one believes in the Big Bang theory. Only CDM leads to clumping and therefore to the formation of galaxies and so on. Examples for CDM are barionic massive compact halo objects (MACHOS) or non-barionic weakly interacting massive particles (WIMPs). Already barionic dark matter has been found, e.g. Brown Dwarfs and other MACHOS can be discovered by gravitational lensing. But the barionic dark matter is not enough to account

for the whole amount of missing mass. Therefore non-barionic dark matter has to exist. Many theories account for WIMPs and therefore WIMPs are among the non-barionic dark matter particles, which are searched for the most.

In the following section the WIMPs, that appear in a theory called Supersymmetry, are described. Supersymmetry itself is shortly introduced and how a signal of supersymmetric dark matter can appear in γ-rays.

3 Supersymmetric Dark Matter

3.1 Introduction to Supersymmetry

3.1.1 Motivation

Nature seems to has a favour for symmetries. A butterfly, a flower or a snowflake are all built symmetrically. But also at the level of fundamental particles symmetries are needed to describe there interactions. They are described by the standard model of particle physics. The standard model of particle physics (standard model from now on) is built upon the gauge principle, which is a symmetry requirement. Quantum field theories, e.g. Quantumelectrodynamics, can be derived by requiring invariance under a local symmetry transformation. The other important mechanism in the standard model is spontaneous symmetry breaking. So assigning a vacuum expectation value different from zero to the Higgsfield, which is spontaneous symmetry breaking, ends up giving masses to some of the particles of the standard model. Hence the Higgsfield is an everywhere existing field needed to give masses to particles. But even though the standard model is in very good agreement ([7]) with a lot of experiments, there are phenomena, e.g. neutrino oscillations ([12]), and problems within the standard model, e.g. the hierarchy problem ([13]), indicating the need of a theory beyond the standard model. As there are many scientists devoted to this subject, many theories, which offer explanations for those phenomena exist. One of these theories is Supersymmetry, which is described in the following.

3.1.2 Supersymmetry Basics

An additional symmetry

The theory of Supersymmetry introduces an additional symmetry to the symmetries of the standard model. It predicts a symmetry between fermions, whose spin is half-integral, and bosons, whose spin has integer numbers. A supersymmetric transformation turns a fermionic state into a bosonic state and vice versa [13]. In terms of the operator Q generating this transformation it is expressed with

$$Q|Boson\rangle = |Fermion\rangle,\ \ Q|Fermion\rangle = |Boson\rangle. \tag{3.1}$$

Here and in the following the N = 1 Supersymmetry is studied. N refers to the number of supersymmetries or distinct copies of Q and $Q^\dagger$. The symmetry between bosons and fermions also implies, that for every standard model particle at least one superpartner exists. The names of these superpartners are generated by adding an "S" at the front of a fermions name, so e.g. the superpartner of the electron is the Selectron. On the other hand the names of the fermionic superpartners of the gauge bosons are generated by attaching an "-ino", e.g. photon and photino. In Table 3.1 all the standard model particles and their superpartners are given. The particles given in Tab. 3.1 are the minimal number necessary to have Supersymmetry. Therefore models based on this set of particles are called minimal supersymmetric models. One is the MSSM, the minimal supersymmetric standard model.

Standard model	Name	Spin	Superpartner	Name	Spin
ν_e, ν_μ, ν_τ	Neutrinos	$\frac{1}{2}$	$\tilde{\nu_e}$, $\tilde{\nu_\mu}$, $\tilde{\nu_\tau}$	Sneutrinos	1
e	Electron	$\frac{1}{2}$	$\tilde{e}$	Selectron	1
μ	Muon	$\frac{1}{2}$	$\tilde{\mu}$	Smuon	1
τ	Tauon	$\frac{1}{2}$	$\tilde{\tau}$	STauon	1
u,d,s,c,t,b	Quarks	$\frac{1}{2}$	$\tilde{u}$,$\tilde{d}$,$\tilde{s}$,$\tilde{c}$,$\tilde{t}$,$\tilde{b}$	Squarks	1
γ	Photons	1	$\tilde{\gamma}$	Photino	$\frac{1}{2}$
Z	Z-Boson	1	$\tilde{Z}$	Zino	$\frac{1}{2}$
W^+,W^-	W bosons	1	$\tilde{W^+}$,$\tilde{W^-}$	Winos	$\frac{1}{2}$
g	Gluons	1	$\tilde{g}$	Gluinos	$\frac{1}{2}$
H_2^+,H_1^-,H_2^0,H_1^0	Higgs	1	$\tilde{H_2^+}$,$\tilde{H_1^-}$,$\tilde{H_2^0}$,$\tilde{H_1^0}$	Higgsinos	$\frac{1}{2}$

Table 3.1: All standard model particles and their superpartners.

Viewing Tab.3.1, it has to be mentioned that the photon γ and the Z-boson are actually made up from a mixture of the B-boson and the W^0-Boson through the electroweak-symmetry breaking according to the Glashow-Weinberg-Salam theory of weak interactions [14]. The corresponding superparters to the B- and the W^0-Boson are the Bino and the additional neutral Wino.
Naturally the question rises whether any of these superpartner particles has been detected yet. Up to now, only standard model particles and no superpartners have

been found experimentally. This implies that Supersymmetry can't be an exact symmetry. An exact symmetry would lead to degenerate masses of the standard model particles and their superpartners. Therefore Supersymmetry needs to be broken to match the experimental results. One of the main motivations for introducing Supersymmetry is the cancellation of the quadratic divergences in the Higgs self coupling, which is the hierarchy or fine-tuning problem (for more details see [13]). This cancelling should be conserved even when the symmetry is broken. The kind of breaking, that takes this into account, is called "soft breaking". In terms of the Lagrangian, this means adding a supersymmetry breaking part $\mathcal{L}_{soft}$ to the supersymmetric Lagrangian $\mathcal{L}_{susy}$. The following part deals with Supersymmetry and the soft breaking of it in terms of the corresponding Lagrangian or the corresponding parts of the Lagrangian. This is still done in the framework of the minimal supersymmetric extension to the standard model (MSSM).
First the standard model Lagrangian is given by:

$$\begin{aligned} L_{std} &= \bar{\Psi}_J(i\not{D})\Psi_J - \frac{1}{4}F^a_{i\mu\nu}F^{ai\mu\nu} \\ &+ \mid D_\mu\phi \mid^2 -V(\phi) \\ &- \lambda_d^{ij}\bar{Q}^i_L \cdot \phi\, d^j_R - \lambda_u^{ij}\epsilon^{ab}\bar{Q}^i_{La} \cdot \phi^\dagger_b u^j_R - \lambda_l^{ij}\bar{E}^i_L \cdot \phi\, e^j_R + h.c. \end{aligned} \tag{3.2}$$

The Einstein sum convention is used here, i.e. i runs over the three factors of the gauge group and J over the various chiral fermions, which are represented by the fields Ψ_J, a is the colour index. ϕ represents the scalar Higgs field. The Q^i_L are the three doublets of left handed quarks, while u^j_R and d^j_R represent the right handed quarks. E^i_L and e^j_R are the left and right handed leptons respectively. The λs are couplings in form of complex valued matrices and 'h.c.' are the hermitian conjugated terms [14]. In Equation 3.2 the three sectors within the standard model are visible. The first line is the gauge sector, the first term describes the interactions between the particles (Ψ and $\bar{\Psi}$) and the gauge forces (in $\not{D}$, which is the covariant derivative) while the second term produces gauge self interactions, as $F_{\mu\nu}$ is the Yukawa field strength tensor. The second line corresponds to the electroweak symmetry breaking, as the Higgs potential $V(\phi)$ makes it possible to assign a vacuum expectation value to the scalar Higgs field ϕ. The last line is the Yukawa sector, where the interactions of the particle fields with the Higgs field take place and masses are generated for the particles. There λ is the Yukawa coupling.
The following part (especially the formulae) is (are) based on [13]. The Lagrangian of a Supersymmetry theory contains also the fields of the superpartners. They are expressed in terms of superfields. A superfield is a multiplet (or supermultiplet) containing the fermions and the sfermions or the gauge bosons and the gauginos. These multiplets are divided into chiral supermultiplets and vector supermultiplets [13]. A chiral multiplet is made up from a complex scalar field with spin 0, rep-

resenting the squarks or sleptons, and a left-handed Weyl spinor with spin 1/2, representing the matter particles like quarks and leptons. A vector multiplet on the other hand contains a real vector field with spin 1 being the gauge boson and a Majorana spinor with spin 1/2 being the corresponding gaugino [18]. A Majorana particle is it's own antiparticle. Now all the standard model fermions need to be put into such muliplets. It turns out that only chiral supermultiplets can account for the standard model fermions. The standard model fermions all have left- and right-handed parts, that transform differently under the gauge group. This property can only be described by chiral supermultiplets. Vector supermultiplets are not possible. Hence for every standard model fermion a chiral multiplet, which also contains the sfermion as a complex scalar field, exists. The gauge bosons of the standard model on the other hand are as mentioned above well suited for the vector supermultiplets. The Higgs boson is a special case. It has spin 0 instead of spin 1 like the other bosons. It is included in a chiral supermultiplet. But actually one chiral supermultiplet is not enough, due to the fact that the fermionic partner of the Higgs chiral supermultiplet would not cancel the gauge anomalies in the electroweak sector. These anomalies are due to the hypercharge of the fermionic partner of the Higgs (Y = 1/2 or Y = -1/2). This hypercharge does not cancel except a second Higgs chiral supermultiplet with opposite sign in the hypercharge of the fermionic partner is present. Furthermore to generate the masses of the up-type quarks with charge +2/3 one Higgs supermultiplet is needed. To generate the masses of the down-type quarks with charge -1/3 and the charged leptons an additional Higgs supermultiplet is necessary. This adds up to two Higgs supermultiplets. This is also seen in Table 3.1. There are four standard model Higgs particles (H_2^+,H_1^-,H_2^0,H_1^0) and also four Higgsinos ($\tilde{H_2^+}$,$\tilde{H_1^-}$,$\tilde{H_2^0}$,$\tilde{H_1^0}$). The notation used there is according to the weak isospin components ($T_3 = 1/2, -1/2$). The Higgs $\mathrm{SU}(2)_L$-doublet complex scalar field, that gives masses to the up-type quarks, is called H_2 (sometimes also H_u). Its weak isosoin components with $T_3 = 1/2$ and $T_3 = -1/2$ are denoted H_2^+ and H_2^0 according to the electric charges +1 and 0. The other Higgs field, that gives masses to the down-type quarks and the charged leptons is called H_1 and its weak isospin components are H_1^0 and H_1^-. The standard model Higgs boson is then a linear combination of the two neutral components H_1^0 and H_2^0. Now a supersymmetric Lagrangian can be written as a sum of the separate Lagrangians for a chiral supermultiplet and a vector supermultiplet and some additional possible interaction terms. This is the following equation:

$$\mathcal{L} = \mathcal{L}_{chiral} + \mathcal{L}_{vector} - \sqrt{2}g(\phi^* T^a \psi)\lambda^a - \sqrt{2}g\lambda^{\dagger a}(\psi^* T^a \phi) + g(\phi^* T^a \phi)D^a \quad (3.3)$$

There ϕ is a complex scalar and ψ is a left-handed Weyl fermion as contained in the chiral multiplet. A massless gauge boson field A_μ^a and a two-component Weyl fermion gaugino λ^a are the components of the vector multiplet. The D^a is

a real bosonic auxiliary field satisfying the equation of motion $D^a = -g(\phi^* T^a \phi)$. This Auxiliary field is an invented field, that allows the symmetry algebra to close off-shell [13]. Finally the T^a stands for hermitian matrices representing the corresponding gauge group. For completeness in the following also $\mathcal{L}_{chiral}$ and $\mathcal{L}_{vector}$ are given in the following.

$$\mathcal{L}_{chiral} = -D^\mu \phi^{*i} D\mu\phi_i - i\psi^{\dagger i}\bar{\sigma}^\mu D_\mu \psi_i - \frac{1}{2}\left(W^{ij}\psi_i\psi_j + W^*_{ij}\psi^{\dagger i}\psi^{\dagger j}\right) - W^i W^*_i \quad (3.4)$$

In Eq. 3.4 the first two terms are the free Lagrangian with the gauge covariant derivative D^μ, while the other terms are the interaction terms. They are defined by the superpotential W via the relations

$$W^{ij} = \frac{\delta}{\delta\phi_i \delta\phi_j} W \text{ and } W^i = \frac{\delta W}{\delta \phi_i} \quad (3.5)$$

The Lagrangian for the vector multiplets reads

$$\mathcal{L}_{vector} = -\frac{1}{4} F^a_{\mu\nu} F^{\mu\nu a} - i\lambda^{\dagger a}\bar{\sigma}^\mu D_\mu \lambda^a + \frac{1}{2} D^a D^a \quad (3.6)$$

where $F^a_{\mu\nu} = \partial_\mu A^a_\nu - \partial_\nu A^a_\mu + g f^{abc} A^b_\mu A^c_\nu$ is the Yang Mills field strength and $D_\mu \lambda^a = \partial_\mu \lambda^a + g f^{abc} A^b_\mu \lambda^c$ the covariant derivative of the gaugino field. In the following the explicit superpotential for the minimal supersymmetric standard model (MSSM) is shown, Eq. 3.7 . There and in the following the notations follow [15]. This means the formula are expressed in terms of the superfields and not as above in terms of the superfield components, the bosonic and fermionic fields [13] .

$$W = \epsilon_{ij}\left(-\hat{\mathbf{e}}^*_R \mathbf{Y}_E \hat{\mathbf{l}}^i_L \hat{H}^j_1 - \hat{\mathbf{d}}^*_R \mathbf{Y}_D \hat{\mathbf{q}}^i_L \hat{H}^j_1 + \hat{\mathbf{u}}^*_R \mathbf{Y}_U \hat{\mathbf{q}}^i_L \hat{H}^j_2 - \mu \hat{H^i_1} \hat{H^j_2}\right) \quad (3.7)$$

The superfields, that turn up within the superpotential W, are all chiral supermultiplets as no gauge bosons besides the Higgs are included.
Now in order to break Supersymmetry the soft Supersymmetry breaking term has to be added to the superpotential W. In the minimal supersymmetric framework the soft Supersymmetry breaking potential looks like the following:

$$\begin{aligned}
V_{soft} = \quad & \epsilon_{ij} \quad \left(-\tilde{\mathbf{e}}^*_R \mathbf{A}_E \mathbf{Y}_E \tilde{\mathbf{l}}^i_L \tilde{H}^j_1 - \tilde{\mathbf{d}}^*_R \mathbf{A}_D \mathbf{Y}_D \tilde{\mathbf{q}}^i_L \tilde{H}^j_1 + \tilde{\mathbf{u}}^*_R \mathbf{A}_U \mathbf{Y}_U \tilde{\mathbf{q}}^i_L \tilde{H}^j_2 + h.c.\right) \\
& - \quad \epsilon_{ij}\left(B\mu \tilde{H^i_1} \tilde{H^j_2} + h.c.\right) \\
& + \quad H^{i*}_1 m^2_1 H^i_1 + H^{i*}_2 m^2_2 H^i_2 \\
& + \quad \tilde{\mathbf{q}}^{i*}_L \mathbf{M}^2_Q \tilde{\mathbf{q}}^i_L + \tilde{\mathbf{l}}^{i*}_L \mathbf{M}^2_L \tilde{\mathbf{l}}^i_L + \tilde{\mathbf{u}}^{i*}_R \mathbf{M}^2_U \tilde{\mathbf{u}}^i_R + \tilde{\mathbf{d}}^{i*}_R \mathbf{M}^2_D \tilde{\mathbf{d}}^i_R + \tilde{\mathbf{e}}^{i*}_R \mathbf{M}^2_E \tilde{\mathbf{e}}^i_R \\
& + \quad \frac{1}{2} M_1 \tilde{B}\tilde{B} + \frac{1}{2} M_2 \left(\tilde{W}^3 \tilde{W}^3 + 2\tilde{W}^+ \tilde{W}^-\right) + \frac{1}{2} M_3 \tilde{g}\tilde{g}
\end{aligned}$$

Here the first line contains the trilinear couplings. Second and the third line are the Supersymmetry-breaking contributions to the Higgs potential, while the fourth line consists of the mass terms for the squarks and sleptons. The last line then finally corresponds to the masses of the bino, the wino and the gluino respectively. The indices i and j are $SU(2)$ indices and $\epsilon_{12} = +1$ (ϵ_{ij} being the Levi-Civita Symbol) defines the sign convention. The quantities $\mathbf{Y}$, the Yukawa couplings, $\mathbf{A}$, the soft trilinear couplings and $\mathbf{M}$ are 3×3 matrices in generation space, while $\hat{\mathbf{e}}$, $\hat{\mathbf{l}}$, $\hat{\mathbf{u}}$, $\hat{\mathbf{d}}$ and $\hat{\mathbf{q}}$ are the superfields described above, which contain the quarks and squarks, the leptons and sleptons. Their scalar components are marked by a tilde and the L and R subscripts on the sfermions correspond to the chirality of their fermionic superpartners. The gaugino fields are also indicated by a tilde over the referring gauge field as shown in Table 3.1. B is a soft bilinear coupling. The mass parameters important to mention are μ as the Higgsino mass parameter, M_1, M_2 and M_3 as the gaugino mass parameters and m_1^2 and m_2^2, which are Higgs mass parameters. These are a lot of free parameters, in total 105. Therefore in most models certain assumptions are made, that reduce the number of free parameters. Two models, the pMSSM (the phenomenological minimal supersymmetric extension standard model) and the mSUGRA (minimal supergravity) model are explained in the next section.

An additional quantum number

The Supersymmetry solves the hierarchy problem. Additionally it effects the decay mechanisms of the standard model. Here a good example is the proton decay, see Fig. 3.1. The decay is not allowed in the standard model, because of baryon and lepton number violation. With Supersymmetry the decay is possible, because it can be mediated by e.g. a squark. The possible decay is shown in Fig. 3.1. Furthermore in Supersymmetry the theoretical lifetime of the proton is too short compared to experiments [16]. An elegant way of solving these problems is the introduction of a new conserved quantum number $R = (-1)^{3\cdot(B-L)+2S}$, where B is baryon- and L lepton number and S the spin. This quantum number is named R-Parity. Every standard model particle has $R = 1$ and every supersymmetric state has $R = -1$. R-Parity is conserved if $\prod R = 1$ at each vertex in a corresponding Feynman diagram. With this law the proton decay as depicted in Fig. 3.1 is forbidden.

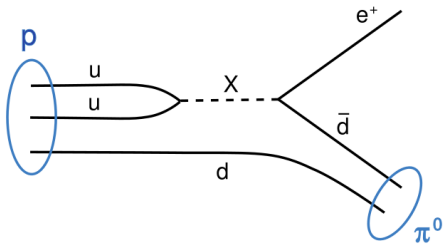

Figure 3.1: The proton decay mediated by e.g. a squark X.

3.2 pMSSM and mSUGRA

In this section two possible supersymmetric models and their parameters are shown. The models are the phenomenological minimal supersymmetric standard model (pMSSM) and the minimal supergravity model (mSUGRA). Calculations for those models can be done with DarkSUSY5.0.1. [3] (with the right interface to other programs). The DarkSUSY5.0.1 package is a tool to perform numerical calculations of supersymmetric dark matter. More on DarkSUSY5.0.1 and the other programs (SUSPECT and ISASUGRA) needed to calculate properties of supersymmetric models, is given in the Appendix. The explanation of the two supersymmetric models is given in the following.

The first model to be explained is the phenomenological minimal supersymmetric extension to the standard model, called pMSSM. The pMSSM, like the MSSM, requires the existence of 32 superpartners to the standard model particles: 12 squarks, 9 sleptons, 2 Winos, 4 Zinos, 1 gluino and 4 Higgs bosons. This is actually the minimal possible particle content if going to Supersymmetry. It was described in the section above that Supersymmetry is softly broken. In order to reduce the large amount of free parameters from 105 to less than 20 constraints for them have to be found. In the pMSSM constraints are appplied, which are motivated by different experiments. First it is assumed that no new sources of CP-violation appear in Supersymmetry, this is motivated by e.g. experiments on the K system, which limit the possibility for the existence of new CP-violation [17]. A further reduction of the free parameters is achieved with the assumption that no flavor changing neutral currents exist in the pMSSM. According to this the mass matrices of the sfermions as well as the trilinear coupling matrices are assumed to be diagonal. A third point in limiting the free parameters is the universality of the first and second order particle generation. Therefore the soft supersymmetry breaking masses of the first and the second generation squarks are chosen to be the same and the trilinear

coupling can even be chosen to be zero. In the end 19 free parameters remain out of the 105. They are $\tan\beta = v_2/v_1$, which is the ratio between the two Higgs vacuum expectation values (vevs), the mass of the pseudoscalar Higgs boson, then the Higgs-Higgsino mass parameter, the bino, wino and gluino mass parameters, then five mass parameters each for the first (which equals the second) generation of sfermion masses and the third generation of sfermion masses and three third generation trilinear couplings.
The second supersymmetric model includes also gravity, as already the name minimal supergravity, mSUGRA, points out. First of all, when taking into account an additional force the particles associated with it have to be introduced. In case of gravitation the graviton and the gravitino have to be studied. But these particles (fields) actually appear naturally if one goes to local Supersymmetry [18]. The main idea, which is used to reduce the parameters in this case, is the unification of forces at very high energies, at the grand unification (GUT) scale. This unification is visible in the running of the coupling constants, α_{elmag}, α_{strong} and α_{weak}. If today measurement of the couplings are extrapolated to the GUT scale unification is not achieved, as shown in Fig.3.2 on the left. But with Supersymmetry the couplings (and masses) unify to an acceptable amount at the GUT scale (10^{16} eV), shown in Fig.3.2 on the right. Therefore at the GUT scale beside the unification of the couplings to a single coupling α also a unification of the gaugino masses to $m_{1/2}$, of the scalar (sfermion and Higgs) masses to m_0 and of the trilinear couplings to A_0 is assumed. Considering the numbers of free parameters of minimal supergravity at the GUT scale, there are only five parameters, or four parameters and a sign, left, which are m_0, $m_{1/2}$, A_0, $tan\,\beta$ and μ. These are the parameters that determine the low energy behaviour of the theory, which is determined by solving the RGEs. This is done in SUSPECT and DarkSUSY uses the results (for more details see appendix).

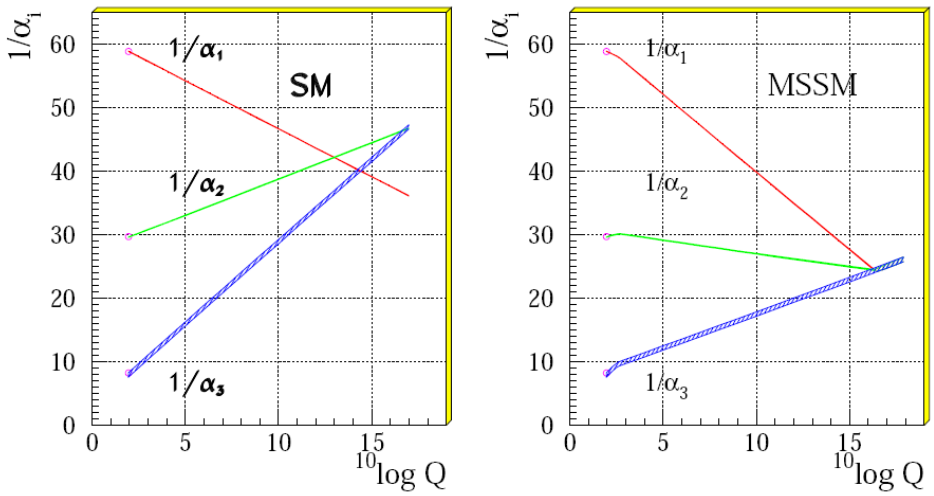

Figure 3.2: The running of the inverse coupling constants is shown. On the left for the standard model and on the right with Supersymmetry (MSSM).

3.3 Dark Matter Candidates

The particles, which qualify as dark matter candidates, turn up quite naturally in Supersymmetry. In order to be a dark matter candidate a particle has to satisfy the following conditions:

1. It do not interact electromagnetically, because there does not exist any direct proof of such particles. Their existence is only revealed through gravitational effects and they are stable.
2. The particle has to be heavy, because only a heavy particle leads to the clumping assumed by big bang cosmologies. This kind of dark matter is also called cold dark matter (see section 1. Evidence for Dark matter)

Particles with these properties are called WIMPs, weakly interacting massive particles. The particles in Supersymmetry, that satisfy these requirements are the so called neutralinos χ_i^0. Neutralinos are linear combinations of the Bino, B, the Wino, W_3 and the neutral Higgsinos, H_1^0 and H_2^0. Generating the mass matrix (Eq. 3.8) in this basis (B, W_3, H_1^0, H_2^0) and diagonalising it (Eq. 3.9) reveals the masses

and compositions of four mariorana states ([15]).

$$M_{\tilde{\chi}^0_{1,2,3,4}} = \begin{pmatrix} M_1 & 0 & -\frac{g' v_1}{\sqrt{2}} & +\frac{g' v_2}{\sqrt{2}} \\ 0 & M_2 & +\frac{g v_1}{\sqrt{2}} & -\frac{g v_2}{\sqrt{2}} \\ -\frac{g' v_1}{\sqrt{2}} & +\frac{g v_1}{\sqrt{2}} & \delta_{33} & -\mu \\ +\frac{g' v_2}{\sqrt{2}} & -\frac{g v_2}{\sqrt{2}} & -\mu & \delta_{44} \end{pmatrix} \tag{3.8}$$

In Eq. 3.8 g and g' are gauge coupling constants of the SU(2) and U(1) gauge group. M_1 is the mass of the bino, while M_2 is the mass of the wino. v_1 and v_2 represent the Higgs vevs. The δs resemble the most important one loop corrections, which can affect the neuralino masses slightly (by a few GeV). Finally μ is the Higgsino mass parameter. The four Majorana states are given in Eq. 3.9. They are distinguished by $i = 1$, 2, 3,4 according to each state. The states are ordered by the masses. $\tilde{\chi}^0_1$ is the lightest neuralino and $\tilde{\chi}^0_4$ the heaviest. The Ns in Eq. 3.9 are complex factors, which are different for each state i.

$$\tilde{\chi}^0_i = N_{i1}\tilde{B} + N_{i2}\tilde{W}^3 + N_{i3}\tilde{H}^0_1 + N_{i4}\tilde{H}^0_2 \tag{3.9}$$

These four states are all neutral and heavy, at least heavier than the standard model particles. But only if the lightest neutralino also is the lightest supersymmetric particle (LSP) it is a dark matter candidate. But also other particles like e.g. the gravitino can turn out to be the LSP. In this case they would be the dark matter candidate, i.e. if the LSP is not interacting electromagnetically, it is a dark matter candidate. That is due to a feature mentioned before, to the conservation of R-Parity. As a consequence the lightest supersymmetric particle is stable. It can not decay into lighter particles, because this would mean decaying directly into two standard model particles, which is forbidden by R-Parity conservation. In the following the case, where the lightest neutralino χ^0_1 is the LSP is studied.
The neutralino χ^0_1 can self annihilate. This is possible, because of the neutralino being a Majorana particle and hence it's own antiparticle. But such an annihilation is only mediated through the weak force. Therefore the cross section for the annihilation is very low. Hence the lightest neutralino χ^0_1 is a very promising dark matter candidate, fulfilling all the requirements. So from now on the dark matter particle is the lightest neutralino χ^0_1.

3.4 Annihilation signals from supersymmetric dark matter

This section is meant to give an overview over the theoretically expected signals, that can be measured on earth when a supersymmetric dark matter particle decays somewhere in the galaxy.

3.4.1 Annihilation of supersymmetric dark matter

The annihilation process of two neutralinos is schematically shown in Fig. 3.3. As mentioned before the neutralino can not decay due to R-parity conservation. But the neutralino is a Majorana particle and therefore it can self annihilate. There are 8 "fundamental" annihilation channels used for the calculation of annihilation products in DarkSUSY5.0.1 ([15]):
$c\bar{c}$, $b\bar{b}$, $t\bar{t}$, $\tau^+\tau^-$, W^+W^-, Z^0Z^0, gg and $\mu^+\mu^-$.
The annihilation into light fermions is helicity suppressed. This suppression is actually cancelled if an additional photon appears in the final state. This is the case for internal Bremsstrahlung, which is discussed in the section on the gamma-ray flux.
The particles created by the annihilation decay soon into lighter particles mostly pions and kaons. In the decays of these particles gammas, neutrinos and also charged particles are produced. For example a positively charged pion, π^+, decays into a muon, μ^+, and a muon neutrino,ν_μ. A neutral pion decays mainly into two gammas, $\gamma\gamma$, but also the decay into one gamma and an electron positron pair, $\gamma\, e^+e^-$, is possible.

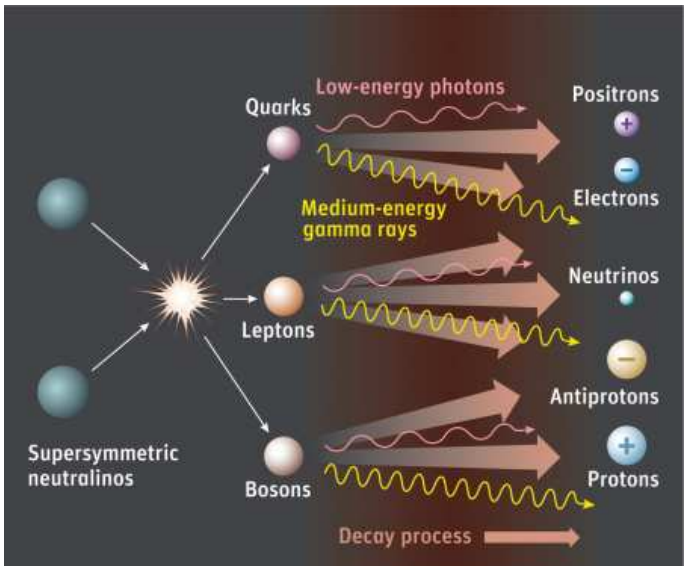

Figure 3.3: Illustration of neutralino annihilation [6]

Of special importance for the following is also the decay of the neutralinos into two photons. Therefore the Feynman diagrams for this process are shown in Fig. 3.4. It can be clearly seen that the annihilation into two gammas is a second order process.

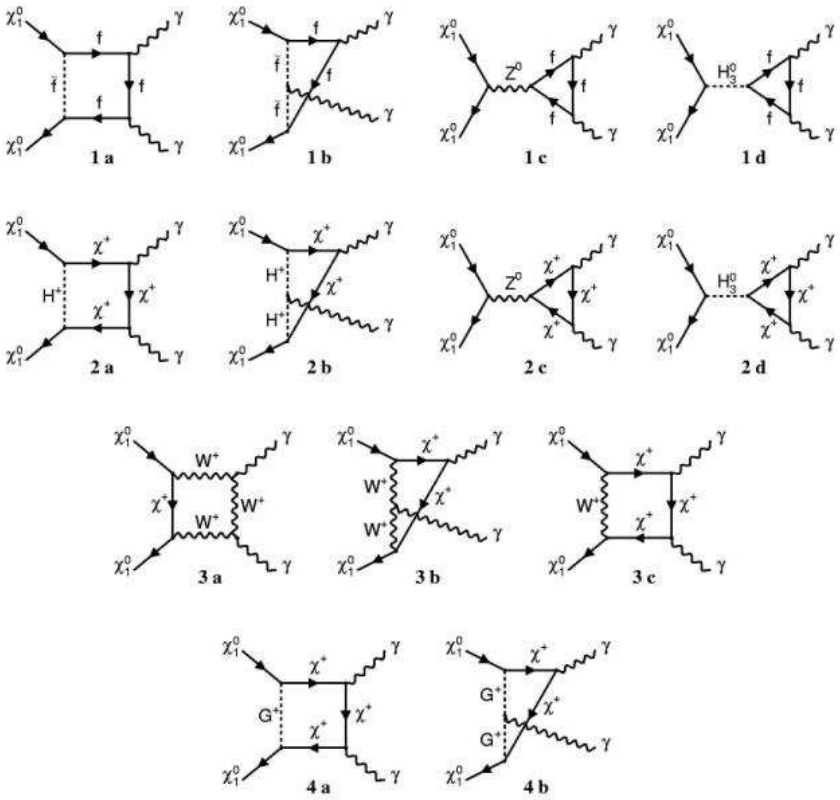

Figure 3.4: Feynman diagrams for the decay of neutralinos into two gammas

3.4.2 Distribution of dark matter in (our) galaxies(y)

Any signal from the annihilation of dark matter particles depends on the density (actually the squared density) of the particles at the position, where the annihilation takes place. The higher the density at that certain position the more dark matter particles annihilate there. Hence the higher the density the stronger the signal. Therefore it is important to know the distribution of the dark matter particle density in our galaxy. A lot of studies exists, in which dark matter density profiles are given, e.g. [20]. These profiles are based on many body simulations but also on fits to rotation curves and fits to lensing (compare Section 1). All profiles are spherically symmetric with respect to the galactic centre. So they are given in terms of $\rho(r)$, where r is the distance to the galactic centre. A very popular profile is the Navarro-Frenck-Withe profile, NFW profile, named after its inventors [21]. While other profiles differ from that they still have the maximum density at the galactic centre. A general form for some possible profiles including the NFW, the isothermal and the Moore profile is given in the following equation

$$\rho(r) = \rho_0 \left(\frac{R_0}{r}\right)^{\gamma} \left[\frac{1+\left(\frac{r}{a}\right)^{\alpha}}{1+\left(\frac{R_0}{a}\right)^{\alpha}}\right]^{\frac{\gamma-\beta}{\alpha}} \tag{3.10}$$

with R_0 being the distance between the earth and the galactic centre, a being a scaling radius and α, β and γ being free parameters. In Fig. 3.5 the NFW profile ($R_0 = 8.0$kpc, $a = 20$kpc, $\alpha = 1$, $\beta = 3$ and $\gamma = 1$), the isothermal profile ($R_0 = 8.5$kpc, $a = 3.5$kpc, $\alpha = 2$, $\beta = 2$ and $\gamma = 0$) and the Moore profile ($R_0 = 8.0$kpc, $a = 28$kpc, $\alpha = 1.5$, $\beta = 3$ and $\gamma = 1.5$) are plotted. So as these profiles all peak at the galactic centre a dark matter signal from this region seems very promising. The other parts of the γ-ray flux (like the cross section or the mass of the dark matter particle, see next section) are independent of the position of the annihilating dark matter particle. Hence only the density points out regions, where dark matter can produce a detectable signal. The profiles discussed so far predict a continuous distribution of the dark matter. But there also exist assumptions that the dark matter makes up clumps, e.g. [22]. The case of a clumpy dark matter halo can also be simulated. One of the above profiles can be chosen and a propability for small dark matter clumps can be added. This leads then to a clumps in the dark matter distribution. In most cases such clumps are expected around centres of gravity, e.g. the centres of galaxies. Such clump scenarios are also derived according to the experimental data (movement of galaxy clusters, gravitational lensing) mentioned above.

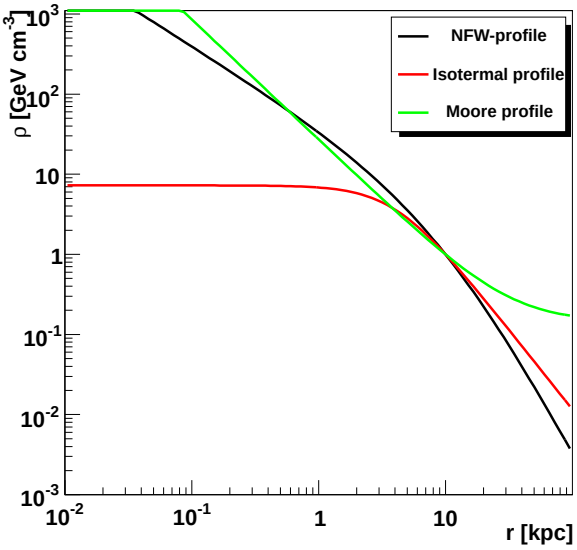

Figure 3.5: Dark matter halo profiles for three different models.

3.4.3 γ-Ray-Flux from supersymmetric dark matter annihilation

In the previous section the importance of the density distribution of dark matter in the galaxy is pointed out. In fact the γ-ray-flux from the annihilation of neutralinos can be expressed in two parts, a astroparticle physics term and a particle physics term. The particle physics term contains the cross section σ. It accounts for the propability of a dark matter particle annihilation. In addition to the cross section also the velocity of the dark matter particle has an impact on this probability and therefore is included in the particle physics term. As mentioned before the density distribution $\rho(r)$ of the dark matter enters the astroparticle physics term. Furthermore the term also takes into account the fact that only the flux from a certain direction is observed. This direction is given by the angle ψ, which is the angle between the direction of the galactic centre and the direction of the target position, where a larger amount of dark matter is expected. A sketch is given in Fig. 3.6. The integrated γ-ray-flux can be expressed with the help of the particle physics term and the astroparticle physics term, Eq. 3.11.

$$\Phi_\gamma(\psi) = \int \frac{d\Phi^{PP}}{dE} \times J^{AP}(\psi) \tag{3.11}$$

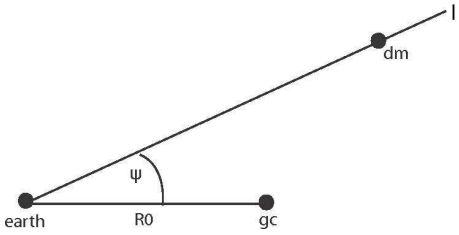

Figure 3.6: The earth the galactic centre (gc) and a dark matter source (dm) are indicated by black circles. The angle ψ is shown. The distance R_0 to the galactic centre and also the length l of the line of sight are given.

The particle physics term $\int \frac{d\Phi^{PP}}{dE}$ is

$$\int \frac{d\Phi^{PP}}{dE} = \frac{N_\gamma \, v\sigma}{4\pi M_\chi^2} \tag{3.12}$$

with $N_\gamma = \int_0^{M_\chi} \frac{dN}{dE}$. The astroparticle physics term $J^{AP}(\psi)$ is a factor depending on the angle ψ

$$J^{AP}(\psi) = \int_{line\,of\,sight} \rho^2(l) dl(\psi) \, . \tag{3.13}$$

Concerning the observation of this flux, the detectors angular resolution $\Delta\Omega$ has to be considered. This is done by averaging $J^{AP}(\psi)$ over this resolution $\Delta\Omega$ (Eq. 3.14).

$$\langle J^{AP}(\psi) \rangle_{\Delta\Omega} = \frac{1}{\Delta\Omega} \int_{\Delta\Omega} d\Omega' J(\psi') \tag{3.14}$$

The whole formula for the integrated flux from the annihilation of dark matter without the angular resolution of a detector can be given by

$$\Phi_\gamma(\psi) = \frac{N_\gamma \, v\sigma}{4\pi M_\chi^2} \int_{line\,of\,sight} \rho^2(l) dl(\psi) \tag{3.15}$$

the factor $1/4\pi$ can be split up and the integrated flux can be rewritten:

$$\Phi(\psi)_\gamma = 1.879 \cdot 10^{-11} \left(\frac{N_\gamma \, v\sigma}{10^{-29} cm^3 s^{-1}} \right) \left(\frac{10GeV}{M_\chi} \right)^2 \langle J(\psi) \; cm^{-2} s^{-1} sr^{-1} \tag{3.16}$$

with $J(\psi) = \frac{1}{8.5\,kpc} \cdot \left(\frac{1}{0.3 GeV/cm^3} \right)^2 \int_{line\,of\,sight} \rho_\chi^2(l) dl(\psi)$. Including the angular acceptance of the detector then yields

$$\begin{aligned} \Phi(\psi, \Delta\Omega)_\gamma \quad &= \quad 1.879 \cdot 10^{-11} \left(\frac{N_\gamma \, v\sigma}{10^{-29} cm^3 s^{-1}} \right) \left(\frac{10GeV}{M_\chi} \right)^2 \cdot \\ &\cdot \quad \langle J(\psi) \rangle_{\Delta\Omega} \times \Delta\Omega \; cm^{-2} s^{-1} sr^{-1} \, . \end{aligned} \tag{3.17}$$

This equation contains different annihilation channels, which are explained in more detail in the following.
For the search for such a signal, special features can be advantages. The decay of the neutralino into two gammas, $\gamma\,\gamma$, and also into $Z^0\,\gamma$ would lead to such a feature. But these decays are loop suppressed, they are second order processes, see Fig. 3.4, and therefore the very nice property of a high single peak at the neutralino mass in the spectrum actually is not visible. Nevertheless recently a new contribution to the γ-ray spectrum has been revealed [23]. It has turned out that Bremsstrahlung, which is the radiation of a photon during the annihilation process, which can be divided into virtual internal Bremsstrahlung (Fig. 3.7 on the right) and final state radiation (on the left and in the middle of Fig. 3.7), adds a significant amount of γ-rays to the total flux. During the annihilation process of neutralinos into leptons and charged gauge bosons the virtual internal Bremsstrahlung dominates over the final state radiation. Not for every model the change in the spectrum caused by internal Bremsstrahlung is large. For some models though there can appear a bump around the neutralino mass, that is not visible without internal Bremsstrahlung. Such a spectrum (with internal Bremsstrahlung) for one specific mSUGRA model (calculated with DarkSUSY5.0.1) is shown in Fig. 3.8. The high flux values at the neutralino mass are then due to internal Bremsstrahlung. The gammas from internal Bremsstrahlung are contributed continuously but peak close to the neutralino mass. The other contributions to the spectrum result mainly from the annihilation channels, that finally lead to the decay of pions or kaons. The γ-rays from these decays are continuously distributed over the energy up the neutralino mass, but with a peak at very low energies. These contributions are called continuous γ rays in the following. In Fig. 3.8 also the impact of the separate components to the whole number of γs is shown. It is taken from [23], where the processes, which lead to internal Bremsstrahlung and also the amount of them are described in more detail.

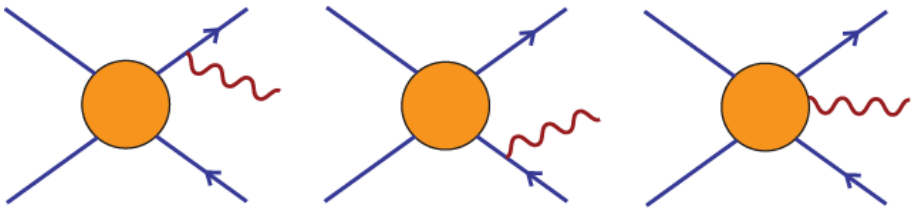

Figure 3.7: Possible Bremsstrahlung processes: The first and the last show final state radiation while in the middle internal Bremsstrahlung is shown.

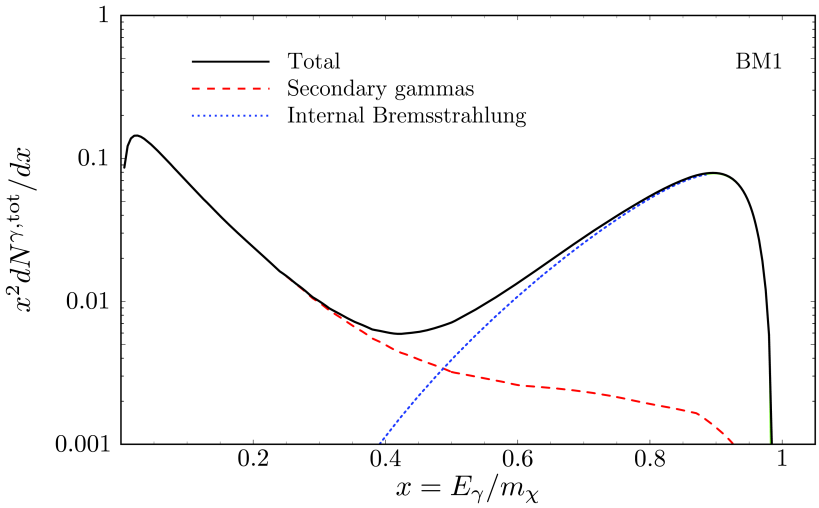

Figure 3.8: Spectrum of a mSUGRA model (BM1) is shown, where the peak caused by Bremsstrahlung is visible. The components creating the spectrum are indicated.

4 H.E.S.S.

This section gives an introduction to gamma-ray astronomy, focusing on the H.E.S.S. Experiment. An overview of the analysis methods used by H.E.S.S. is given. Emphasis is placed on the special requirements for dark matter search.

4.1 Gamma-Ray Astronomy

The sky has been studied by humans for more than 2000 years. For a long time only the photons in the range of the visible light were seen. But in 1912, Viktor Hess discovered the cosmic radiation, which consists of neutral particles, such as photons, but also of charged particles, e.g. electrons and protons. It is known since then, that not only photons with energies in the region of the visible light, but in almost every energy region from a few eV up to 50 TeV exist. But the high energy γ-rays are fully absorbed by the earth's atmosphere, for this reason it is only possible to detect high energy γ-rays with satellites or balloons. Hence γ-ray astronomy did not start until the 1960s, when the first satellites were launched. Nevertheless the interest in high energy γ-rays is immense, because γ-rays unlike charged particles carry information about the direction of their origin. Charged particles are very likely to interact with the interstellar medium and to be deflected by magnetic fields of gas or molecular clouds. Although satellites made first observations of the high energy γ-rays possible, they also are severely limited, because they have a very small detection area. Satellites have strong restrictions on their mass. So a very large detection area as needed for high sensitivity in observing γ-rays can not be offered by a satellite. That's why a ground-based detector is required. The question remains how to solve the problem of the absorption in the earth's atmosphere. In this point, Blankett came up with an idea to indirectly detect the γ-rays via Cherenkov light. His idea was put into reality with the Whipple Telescope in the 1980s. With the Wipple telescope the first Imaging Air Cerenkov Telescope (IACT) started operating [24].
More about the indirect detection of γ-rays through Cerenkov light is explained in the next section.

4.2 Air showers

Whenever a cosmic ray particle, e.g. a proton or a photon, enters the earth's atmosphere it starts an air shower. In the following the processes leading to such an air shower are described for a photon as initial particle. The photon is absorbed in the atmosphere. Thereby the photon initiates a particle shower cascade via the processes of pair production and Bremsstrahlung, in which energy is lost. A simple model (Heitler 1954) for the evolution of such a particle cascade is given in Fig.4.1 and described in the following.

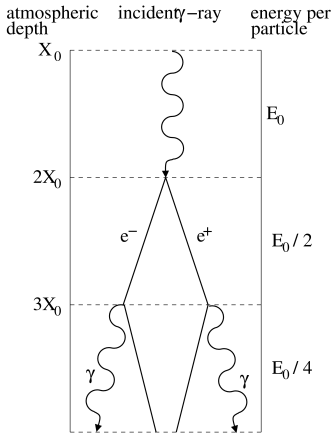

Figure 4.1: Model for the evolution of an electromagnetic air shower.

The photon, after it travelled a mean pathlength X_0, decays to an electron-positron pair. The electron and the positron also travel a mean path length X_0 and then radiate each photons via Bremsstrahlung. These photons, if they still have an energy $E > 2m_e c^2$, again decay in electron-positron pairs. These processes recur until the energy of the photons reaches a critical energy ($E_{crit} \approx 80$ MeV), where Bremsstrahlung is no longer the dominant process of energy loss, but the ionisation of air molecules. So the entering of a high energy photon results in an electromagnetic air shower. Such a shower is given in Fig.4.2 on the left panel. The first interaction leading to the shower generally takes place 15-20 km above sea level and the shower extends to about 8-12 km. Of course not only photons are the primary particles of such an air shower but in principal all the cosmic ray particles are. But hadrons in contrast to other cosmic ray particles do not create electromagnetic showers. They produce hadronic showers. There the main processes of energy loss are more difficult as not only Bremsstrahlung and pair production appear. The differences between a hadronic air shower and an electromagnetic air shower are

the shapes of the showers. A hadronic shower is wider than an electromagnetic shower. This is shown in Fig. 4.2. There a proton-induced shower is shown in the right panel and a photon induced shower on the left panel.
These air showers produce Cherenkov light, which is used to detect the primary particle. How this is done and more on Cherenkov light is given in the next section.

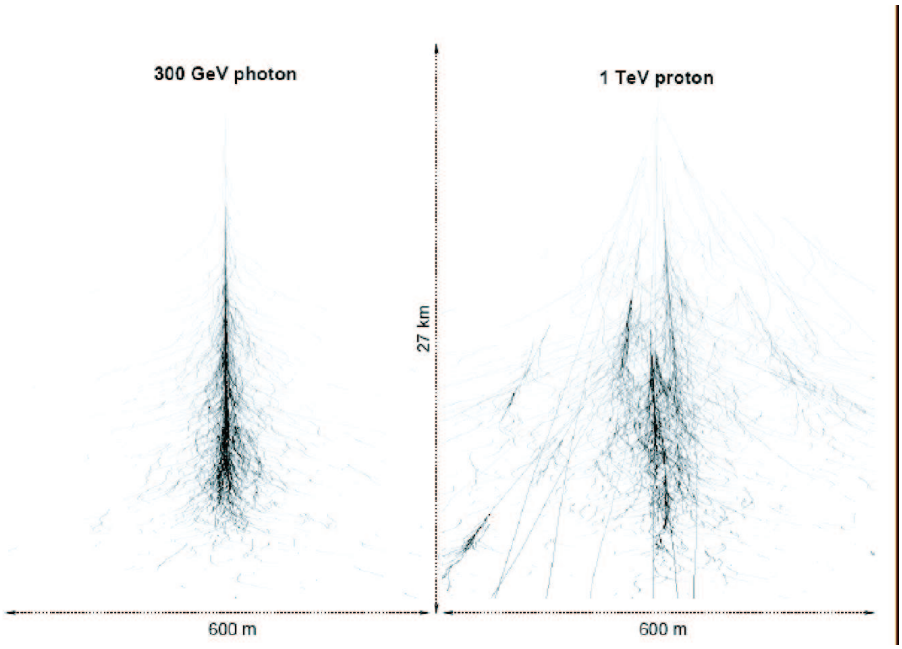

Figure 4.2: Electromagnetic shower induced by a γ (on the left) and a hadronic shower induced by a proton (on the right).

4.3 Cherenkov Light in γ-ray astronomy

Cherenkov light is emitted by charged particles, when they move faster than the speed of light in a certain medium. A charged particle polarises the molecules around it. This results in an electric dipole. When the charged particle moves, the dipole field changes, which leads to the emission of electromagnetic radiation. In case the velocity of the charged particle is smaller than the speed of light in the sourrounding medium ($v < c/n$, n refractive index of the sourrounding medium) the system is symmetric and the dipole of the whole system equals zero. But if $v > c/n$ the dipoles are no longer distributed symmetrically and the dipole of the

whole system changes and emits radiation. This radiation is called Cherenkov light. Cherenkov light, which is blue/ultraviolet ($\lambda \sim 300 - 600\,\mathrm{nm}$), is emitted under a specific angle Θ_c. This angle is calculated to

$$cos(\Theta_c) = \frac{1}{n\beta}\,, \tag{4.1}$$

where $\beta = v/c$, v being the particle's velocity, c the speed of light and n the refractive index of the surrounding medium. In Fig. 4.3 a sketch is shown, which indicates how one can derive the relation given in Eq. 4.1.

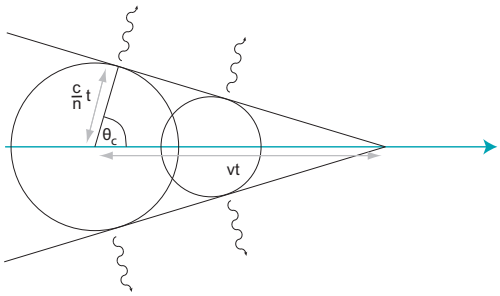

Figure 4.3: Wavefront created by Cherenkov radiation.

The angle Θ_c is given in Fig.4.1. The particle moves a distance $v \cdot t$ in the time t in it's flight direction (horizontal in Fig. 4.3). The light emitted at $t_0 = 0$ under the angle Θ_c moves in the same time t a distance $c/n \cdot t$. The particle emits also light in the time between $t_0 = 0$ and t. This is depicted in Fig. 4.3 with the two circles. The radii correspond to the covered distance of the light emitted at a certain time t ($t_0 = 0$ for the large circle and $t_0 < t_1 < t$). The tangent on this curves then illustrates the wavefront produced by the emitted light due to interference. As described in the section above, air showers are produced by particles entering the earth's atmosphere. A photon, which is neutral and therefore doesn't emit Cherenkov light, decays into electrons and positrons, which are charged. As long as the energy of these decay products is higher than $\mathrm{E}_{min} = \frac{m_e c^2}{\sqrt{1-n^{-2}}}$, they radiate Cherenkov light. In air (with refractive index n= 1.000293) E_{min} for an electron is about 21 MeV. The Cherenkov light is emitted under an angle of about 1° in air. This the leads to an illuminated area on the ground, which is about 250 m in diameter. A telescope, that is situated somewhere in this light pool, can detect the Cherenkov light if enough photons are collected by the telescope mirrors. For an initial photon with an energy of about 1 TeV, 100 photons per m^2 arrive at the ground. They arrive in a very short interval of only a few nanoseconds. In Fig. 4.4, a telescope situated in the lightpool of Cherenkov light from an air shower is shown.

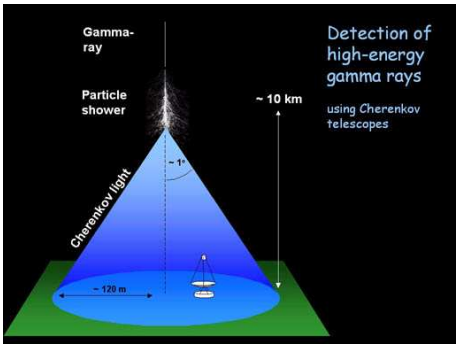

Figure 4.4: Cerenkov light from an airshower illuminating the ground.

The effective detecting area of such a telescope is about 50000 m^2 as it corresponds to the area of the light pool [25]. In Fig.4.5 a sketch of how the light is collected by a mirror in the telescope and then reflected on the camera is drawn. Since the intensity of the Cherenkov light is very low (about 100 photons per m^2 for a 1 TeV energy of the initial photon) large collector areas are needed to collect the Cherenkov light. The reflector in Fig. 4.5 is a very large mirror area. In the focal plane of this mirror a camera is placed. The camera image is then analysed further to gain information about the shower parameters and its origin. This reconstruction is an important part of the analysis and is described in more detail in the section about the H.E.S.S. reconstruction.

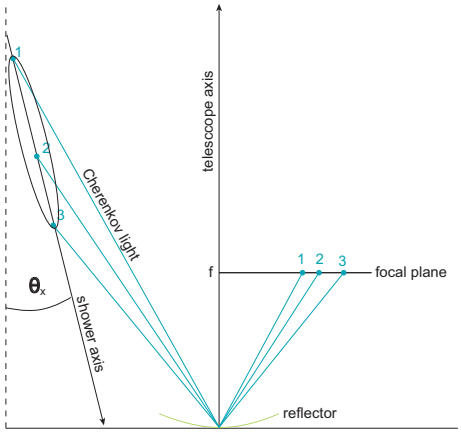

Figure 4.5: Reflection of Cherenkov light from the telescopes mirrors to the camera. The projection on the focal plane of the camera is visible. The way of the light for three points of an ellipse is indicated.

4.4 The H.E.S.S. experiment

The H.E.S.S. experiment (Fig.4.6) is situated in the Khomas Highlands of Namibia near the Gamsberg at 23°16'18" South and 16°30'00" East [28]. This location was chosen due to its very good observation conditions: dark nights, without any clouds, no light from big cities. In addition the southern hemisphere allows to view the galactic plane. The experiment consists of four Imaging Atmospheric Cherenkov Telescopes (IACTs). Hence the system is stereoscopic, which means more than one telescope is used to take data. The four IACTs are placed in a square with a side length of 120 metres. This length is optimised to achieve high sensitivity above 100 GeV. Each telescope has a mirror built up from 380 single mirrors, each with 60 cm diameter. The mirror has an area of 107 m^2. This mirror focus the light to a camera consisting of a hexagonal array of 960 photo-multiplier tubes (PMTs) in the focal plane of the mirror, which is at a distance of 15 meters. The mirrors are arranged on a sphere with radius f. The field of view of the camera is 5°, i.e. each of the 960 PMTs corresponds to an area of 0.16° on the sky. For more information please refer to [28] and the references therein.

Figure 4.6: The H.E.S.S. experiment with the four Imaging Atmospheric Cherenkov Telescopes in Namibia.

4.5 Analysis Methods

The analysis used by H.E.S.S. is described in this section. The triggering, the parametrisation of the camera images recorded and the reconstruction of the shower parameters is explained. In addition, background models and the reconstruction of

a spectrum with a power law with a normalisation F_0 and a photon index Γ are shown.

4.5.1 Trigger

The trigger system consists of three levels. The first two levels could also be used for a non-stereoscopic system, i.e. when only one telescope is taking data. The third trigger, though, explicitly makes use of the data coming from a second (third, fourth) telescope. The first level requires 3 pixels above 4 photo-electrons (p.e.) within a time interval of 1.5 ns in a sector. A sector consists of 64 pixels. In order to trigger the camera, at least three pixels have to have exceeded the singel pixel threshold. The third part of the trigger system requires a coincidence between at least two triggered telescopes. Only if both (all) telescopes trigger within an interval of 80 nanoseconds the cameras of both (all) telescopes are read out.
Since the trigger rate is affected by sky conditions, e.g. clouds or dust, further data quality checks are necessary. Hence certain runs, for which the mean trigger rate is under 70% of the expected value (see [28]) or the rms ... variation of the trigger rate is above 10%, are rejected. Another source affecting the trigger are very bright stars. In order to prevent an over-current of individual PMTs pixels with bright stars in the field of view are identified in advance and turned off. But other light sources such as airplanes, lightning or satellites can also result in triggering the over-current protection, which then leads to a number of PMTs, which are turned off. For this reason, the mean number of PMTs, which are turned off or are simply inactive during a run, is measured and only data, that is taken with less than 10% of the PMTs missing is processed in order to analyse it further.

4.5.2 Image Cleaning

Due to the fact that most pixels contain night sky backround (NSB) and only a few contain the real image, the camera image needs to be cleaned. The cleaning consists of a two-level filter. First the pixels must exceed a lower threshold of 5 p.e.. In addition a neighbour with more than 10 p.e. has to exist and vice versa. The values of the pixels, which don't pass these criteria, are set to zero. This can lead to a spatial correlation of the collected areas. Such a spatial correlation indicates that the image is caused by Cherenkov light from an air shower. After the image cleaning, images of γ-ray-induced showers have a narrow elliptical shape. Background images caused by hadrons, on the other hand, have a wider and more uneven shape.

4.5.3 Hillas Parameters

For further selections the Hillas parameters are used [29]. The Hillas parameters are defined as shown in Fig.4.7. They consist of

- the **width** and **length** of the ellipse,
- the **centre of gravity** and its **distance to the camera centre**,
- the **angle** α, which describes the orientation of the image, and **the brightness of the image**, which is given by the **size** parameter, which is the total number of p.e.s in the image.

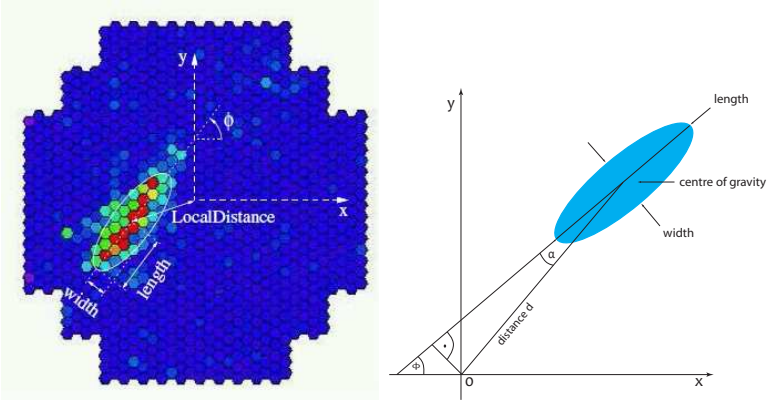

Figure 4.7: Left panel: A camera image. The white contours mark the fitted ellipse and the Hillas parameters are depicted.
Right panel: Schematic illustration of the Hillas parameters in the camera coordinate system.

4.5.4 Cut parameters

First mean scaled quantities are defined. The mean scaled reduced width and length are introduced. The cuts on these parameters are necessary to distinguish between γ-ray events and hadron events. A mean scaled quantity is defined by $p_{tel} = (p - \langle p \rangle)/\sigma_p$, where p is the measured value, $\langle p \rangle$ is the expected value derived from Monte Carlo simulations and σ_p is the expected width of this value depending on the image amplitude, image distance and the zenith angle. The zenith angle is the angle of the telescope pointing. In H.E.S.S., the cuts are applied on the mean reduced scaled width and length (MRSW and MRSL). The mean reduced scaled

width is defined as MSRW = $(\sum_{tel} p_{tel})/N_{tel}$, which is the mean value over all four telescopes. The mean reduced scaled length is defined respectively.
In addition to the MRSW and MRSL, further variables are used as cut parameters. So a cut on the parameter Θ, which is the distance between the reconstructed shower direction (see Section 4.4.4 Reconstruction) and the true direction of the source, is applied in the H.E.S.S. analysis. The selection cuts combine cuts on Θ^2, on the mean scaled parameters, on the image intensity (size) and on the local distance. For different observation conditions, different sets of cuts exist. The standard cuts are optimised for sources having a flux of about 10% of the Crab Nebula and a similar spectrum. The hard cuts are best for sources with a 1% Crab flux and a spectrum with a spectral index $\Gamma = 2.0$. They yield a better significance for weak sources, but also lead to a higher energy threshold. Furthermore, a set of loose cuts is used, giving best results for a strong source similar to the Crab with $\Gamma = 3.0$. The loose cuts lead to a lower energy threshold. The values for these selection cuts are given in Table 4.1.

Parameter	loose	standard	hard
size [p.e.]	>40	>80	>200
local distance max [deg]	2.0	2.0	2.0
MSRL	-2 – 2	-2 – 2	-2 – 2
MSRW	-2 – 1.2	-2 – 0.9	-2 – 0.7
Θ^2 [deg^2]	0.04	0.0125	0.01

Table 4.1: Basic set of selection cuts used in the H.E.S.S. analysis

4.5.5 Shower Reconstruction

For the shower reconstruction in H.E.S.S., it is important that the images are taken in stereo mode. This means that always at least two telescopes have triggered and provide an image. It is straight-forward to reconstruct the impact point, which is the point on the ground hit by the elongated shower axis. It is given by the intersection point of the image axes in the plane perpendicular to the telescopes' pointing directions. The same approach is used to estimate the point of first interaction, the origin of the shower. Therefore the images of the four cameras are superimposed and the intersection point of the main axes is taken to be the origin of the shower. This is illustrated in Fig.4.8.
The energy of the primary particle is obtained from the relation of the particles energy to the recorded signal. This relation is known from Monte Carlo simulations. The energy is then parametrised from these simulations using the image amplitude, the reconstructed impact parameter, which is here the distance from the impact

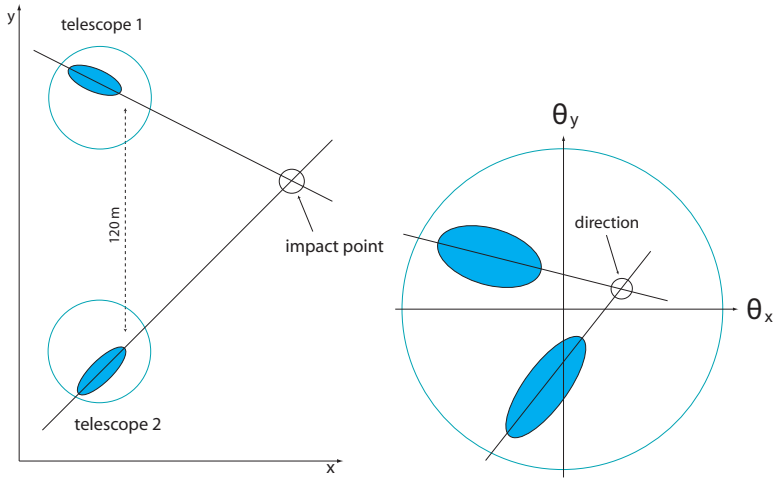

Figure 4.8: Reconstruction of the impact point and the shower direction.

point to the telescope, and the zenith angle of the observation. The reconstructed energy E_{reco} has an error ΔE of about 20% relative to the true energy E_{true}. This is expressed with $\Delta E/E_{true} = (E_{reco} - E_{true})/E_{true}$.

4.5.6 Background models

The H.E.S.S. analysis has several different methods for backround estimations [27]. One possibility is to take so called ON-OFF-runs. The background is estimated by dedicated Off-runs, i.e. the telescope was pointed to a position with no known γ-ray source and similar conditions as the source position (On-region). The disadvantage of this observing method is the loss of On source time. Hence a different observation mode is chosen, which is called wobble-mode. It was first used by the HEGRA collaboration. In the wobble-mode, the source is in the field of view (FOV), but it is offset from the camera centre by typically $\pm$ 0.5°. In general, four runs with changing offset are taken. Having a number N_{on} of On events in a test region and a number N_{off} of Off events in a backround region, the excess in γ-rays is defined as $N_{excess} = N_{on} - \alpha N_{off}$, where the parameter α corrects different acceptances in the two regions and different observation times. In the following, four methods based on this principle, which are used in the H.E.S.S. experiment to estimate the backround, are shown.
One model is the reflected region background model. Here n_{off} off-regions are lying on a ring centred around the test region (see Fig.4.9 on the right panel). Every off-region has the same size and shape as the on-region, as well as the same offset

to the observation position. Because of this α is just $1/n_{off}$. An excess map with the regions of the reflected region background model is shown on the right panel in Fig.4.9.
A more robust method is the ring-background model. Here a circle containing the source position defines the On-region, while a ring around the On-region defines the Off-region. Typically the size of the Off-region is about 7 times the size of the On-region. This results in $\alpha \sim 1/7$. An illustration of this background model is shown on the left panel of Fig.4.9. Further background models are the field-of-view background model and the template background model [27]. But they are not used in the following. Hence they are not explained here in more detail.

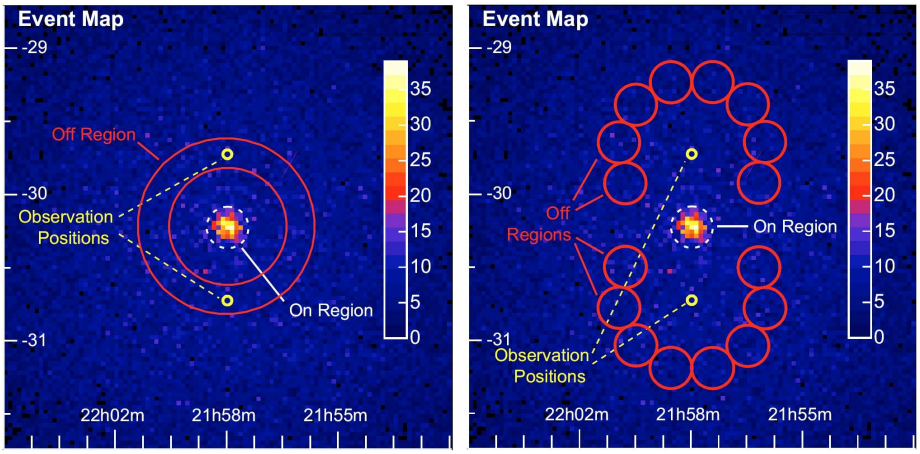

Figure 4.9: On the left, the Ring background model is shown. On the right, the reflected region background model.

4.5.7 Spectrum

In order to derive an energy spectrum from the detected gamma-rays, the number of events, that is lost due to triggers and analysis cuts needs to be taken into account. This number is not known and is therefore derived with Monte Carlo simulations. In addition the detection rate depends on the energy. All these dependencies are put into a parameter called the effective areas $A_{eff}(E)$. With the effective areas $A_{eff}(E)$ the differential spectrum can be expressed by the following:

$$F(E) = \frac{1}{t_{live} A_{eff}(E)} \frac{dN_\gamma}{dE}. \tag{4.2}$$

t_{live} is the live time of the runs. The integral flux is then the integral of Eq. 4.2 over energy above a certain energy threshold of typically around 1 TeV. In the following effective areas the parameters they depend on are looked at more closely.

4.5.8 Effective areas

The effective areas are calculated with Monte Carlo simulations. They depend on the zenith angle α_{zen} and also on the offset Θ and the energy of the shower. Furthermore, they depend on the azimuth angle ϕ of the telescope pointing. The effective areas are calculated by:

$$A_{eff}(E_{rec}, \alpha_{zen}, \Theta, \phi) = \frac{N_\gamma^{sel}(E_{rec}, \alpha_{zen}, \Theta, \phi)}{N_\gamma^{MC}(E_{rec}, \alpha_{zen}, \Theta, \phi)} \cdot A_{eff}^{MC}(E_{rec}, \alpha_{zen}, \Theta, \phi) \tag{4.3}$$

N_γ^{MC} is the total number of gammas generated in the Monte Carlo simulation (MC). N_γ^{sel} is the number of gamma-rays, which passed through the analysis. A_{eff}^{MC} is the simulated area, in which the gammas appeared. Monte Carlo simulations for 13 different zenith angles exist, which are used as look-up tables for the effective areas. These look-up tables are divided into tables for sources located in the south and sources located in the north, because small differences exist between these directions. A decrease in the optical efficiency over the years is taken into account by the generation of a new set of look-up tables, for which a lower optical efficiency is assumed in the simulation. This shifts the energy threshold to slightly higher energies. The energy threshold is derived from a convolution of the effective areas with a power-law spectrum. The maximum of the resulting curve is chosen as energy threshold. Hence the effective areas are closely related to the energy threshold.

5 Search for gamma-rays from supersymmetric dark matter annihilation

Finally the main work of this thesis is presented, which also contains the usage of the programme package DarkSUSY5.0.1. In addition the analysis to receive an upper limit on the velocity weighted cross section of the dark matter particle is shown and a new approach in the search for dark matter is explained.

5.1 Consistency checks with DarkSUSY5.0.1

For most calculations in this thesis the DarkSUSY5.0.1 program package is used. Therefore a good understanding of the program is needed. First an individual self-written programme is developed in order to recalculate some of the DarkSUSY outputs for comparison. The goal of the self-written program is to recalculate the integrated γ-ray flux from the annihilation of supersymmertic dark matter. This is done in the self-written program by the calculation of the two parts, J^{AP} and the particle physics term, of the flux. The astrophysical part J^{AP} itself is then also compared to results obtained with DarkSUSY5.0.1. The parameters needed for the calculation of the integrated γ-ray flux are the full velocity weighted annihilation cross section, the mass of the dark matter particle (the neutralino) and the angular resolution $\Delta\Omega$ of the corresponding detector as shown in the following formula.

$$\begin{aligned}\Phi(\psi,\Delta\Omega)_\gamma &= 1.879\cdot 10^{-11}\left(\frac{N_\gamma\, v\sigma_{X^0\gamma}}{10^{-29}cm^3s^{-1}}\right)\left(\frac{10GeV}{M_\chi}\right)^2 \\ &\quad\cdot\langle J(\psi)\rangle_{\Delta\Omega}\times\Delta\Omega\ cm^{-2}s^{-1}sr^{-1}\end{aligned} \tag{5.1}$$

These parameters, except the angular resolution $\Delta\Omega$, differ from one supersymmetric model to the other. Their values are taken out of calculations done with the DarkSUSY 5.0.1 programme package [15]. The following shortly describes the derivation of the two parts from the self-made programme and the comparison of the results with DarkSUSY.

As mentioned before the calculation of the integrated γ-ray flux can be separated in two terms. As the particle physics term contains only constants or parameters, which are taken from the DarkSUSY package, the calculation of the Astroparticle physics term in the self-written programme is described in more detail in the following. First the expression for the integral over the line of sight $J(\psi)$ is derived. This integral depends only on the angle ψ. No more parameters are needed, because the dark matter profile is assumed to be spherically symmetric. Hence the geometry of the problem can be viewed in two dimensions, as is shown in Fig. 3.6. There the distance between the earth and the galactic centre is named R_0. Furthermore the position of an arbitrarily chosen dark matter source is indicated by a filled black circle. The angle ψ is given and l is the length of the line of sight over which is integrated. The integral is given by $J(\psi) = \int_{line\,of\,sight} \rho^2_{dm}(r(l))dl$. In order to calculate this, the distance r from the galactic centre has to be determined for every point on the line of sight l. So the dependency between r, l and ψ has to be derived. This is done by using Fig. 3.6. For every distance r(l) the following formula is valid:

$$r(l)^2 = l^2 + R_0^2 - 2 \cdot l \cdot R_0 \cdot cos(\psi) \tag{5.2}$$

This can be used for the calculation of the integral. The integral is then calculated numerically. To check if the parametrisation is right, the result of the integration is compared to results obtained with DarkSUSY in Fig. 5.2. A satisfying agreement of the curves for some different halomodels is seen.

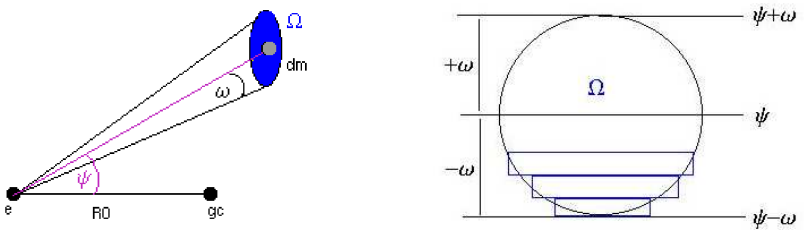

Figure 5.1: On the left the cone originating from the resolution Ω of the detector is sketched. On the right the slices summed up in the calculation of the average over Ω are shown.

The next step is to include the averaging over the angular resolution Ω of the detector. This angular resolution leads to a cone around the initial angle ψ_0. The calculation of the average is just a second integration. It can be interpreted as calculating the area of a circle. The area of this circle is equal to the solid angle

Ω. For a better understanding a sketch is plotted in Fig. 5.1 on the left panel. The area is then calculated by adding up slices of size $\Delta\omega \cdot \Delta\psi$ as shown in Fig. 5.1 on the right panel.
Finally also the results from this very rough estimate are compared to the results gained with DarkSUSY. The two results agree well and eventually the integrated flux can be calculated. Now Eq. 5.2 is calculated for several mSUGRA benchmark

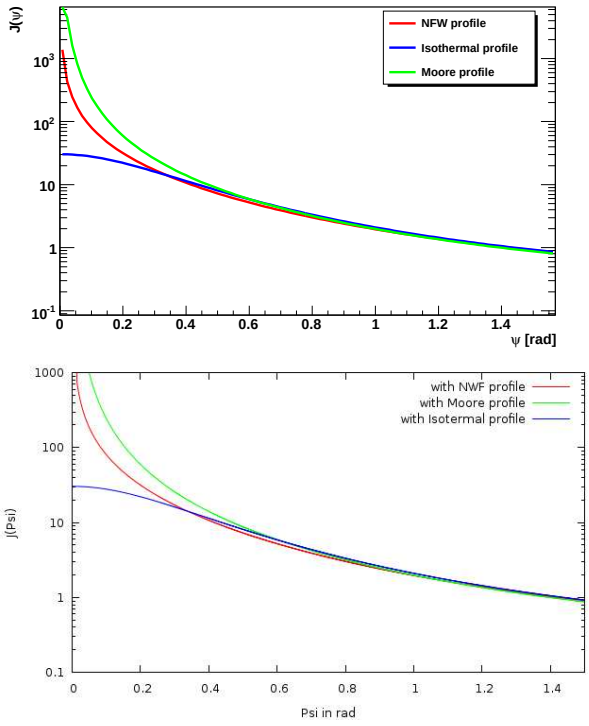

Figure 5.2: On top the calculation of the integral with the self-written program is shown for several dark matter density profiles. On the bottom the same profiles, which are calculated with the DarkSUSY package are plotted. Different models are used for the estimation of the dark matter density profile.

models, see Tab. 5.1. The missing parameters such as σv and m_{DM} are taken from DarkSUSY. The results for the mSUGRA benchmark models (see Table 5.1) are shown in Fig. 5.3. The flux calculated in DarkSUSY5.0.1 is visible in Fig. 5.3 on the right (black dots), while on the left the results from the self-written programme are plotted (blue dots). It is obvious that the results are in good agreement with each other. A minor lack in accuracy concerning the results from the self-written

program is due to the calculation of $J(\psi, \Delta\Omega)$, which is described above. Hence there is room for improvement, though for the ongoing work in this thesis it is regarded unnecessary. As the tests for consistency with DarkSUSY have been successful.

modelname	m_0 in GeV	$m_{1/2}$ in GeV	A_0 In GeV	μ	$tan\,\beta$
BA_AP_000001	107	600	0.0	1	5
BA_BP_000001	57	250	0.0	1	10
BA_CP_000001	80	400	0.0	1	10
BA_DP_000001	101	525	0.0	-1	10
BA_EP_000001	1532	300	0.0	1	10
BA_FP_000001	3440	1000	0.0	1	10
BA_GP_000001	113	375	0.0	1	20
BA_HP_000001	244	935	0.0	1	20
BA_IP_000001	181	350	0.0	1	35
BA_JP_000001	299	750	0.0	1	35
BA_KP_000001	1001	1300	0.0	-1	46
BA_LP_000001	303	450	0.0	1	47
BA_MP_000001	1125	1840	0.0	1	51

Table 5.1: Set of mSUGRA benchmark models

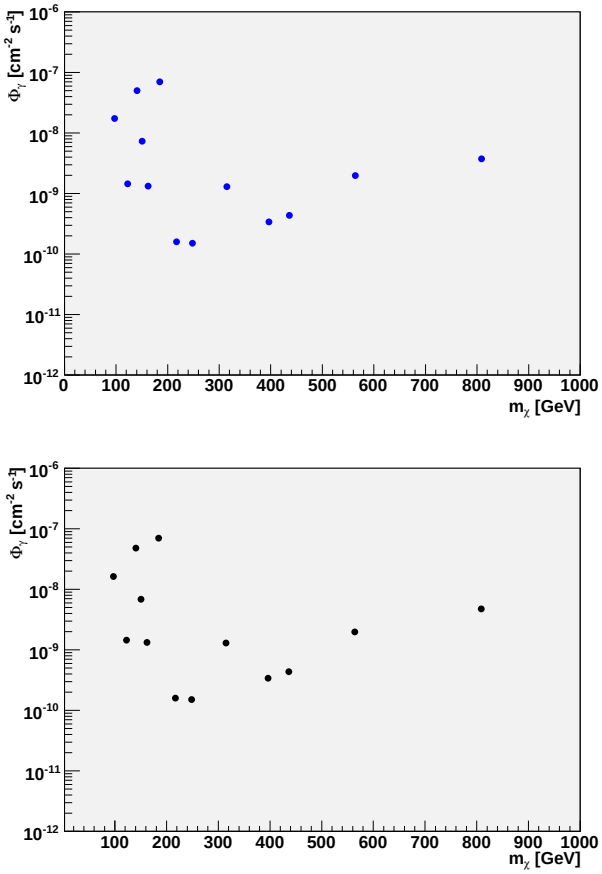

Figure 5.3: On the top panel the integrated γ-ray flux from DarkSUSY5.0.1 is plotted in black dots. On the lower panel the integrated γ-ray flux from the self-made programme is given in blue dots. The mSUGRA benchmark models from Tab. 5.1 have been used here.

5.2 The spectrum at the galactic centre

After gaining a better understanding for the DarkSUSY package, the main objective became the analysis of H.E.S.S. data. In a straight forward approach, the spectrum of the galactic centre measured by H.E.S.S. is compared to spectra of the benchmark models (Tab. 5.1) calculated with DarkSUSY5.0.1. The galactic centre is chosen, because there the density of dark matter is very high. The NFW and also other profiles even predict a peak of the density at the galactic centre. Because of this, the γ-ray flux from dark matter annihilation is highest at the galactic centre. The spectrum of the galactic centre is calculated within the H.E.S.S. software using the wobble chain analysis with the ringbackground and standard cuts (see section 4). The resulting spectrum (together with the dark matter spectra) is shown in Fig. 5.4 on top. It is visible there that the dark matter spectra only reach up to the neutralino masses and that they are not higher than about 1 TeV for the benchmarkmodels. The spectrum of the galactic centre on the other hand goes up to around 14 TeV. This high energy part of the spectrum is certainly not caused by dark matter annihilation as neutralino masses in this range are very unlikely. Also accelerator constraints and constraints derived from the WMAP data favour a less heavy neutralino mass. Hence the important part of the H.E.S.S. spectrum, which is intersting to study, is the low energy part around 1 TeV. Another feature of the dark matter spectrum, which can be seen in Fig. 5.4, is that most models lead to spectra, which are several orders of magnitude to low to be compared with the actual spectrum seen by H.E.S.S.. Also spectra from other regions are compared to the spectra of the different mSUGRA benchmark models from Table 5.1. This is shown also in Fig. 5.4 on the bottom. There the same features can be seen. Therefore it makes no sense to fit any of the H.E.S.S. spectra with a dark matter spectrum. But nevertheless it comes clear that the data analysis has to be optimised for the low energy range about 1 TeV. So in the following these requirement is taken into account, which means that some constraints are applied on the data used for the analysis. One thing to consider are the effective areas, which are described in more detail in the next section.

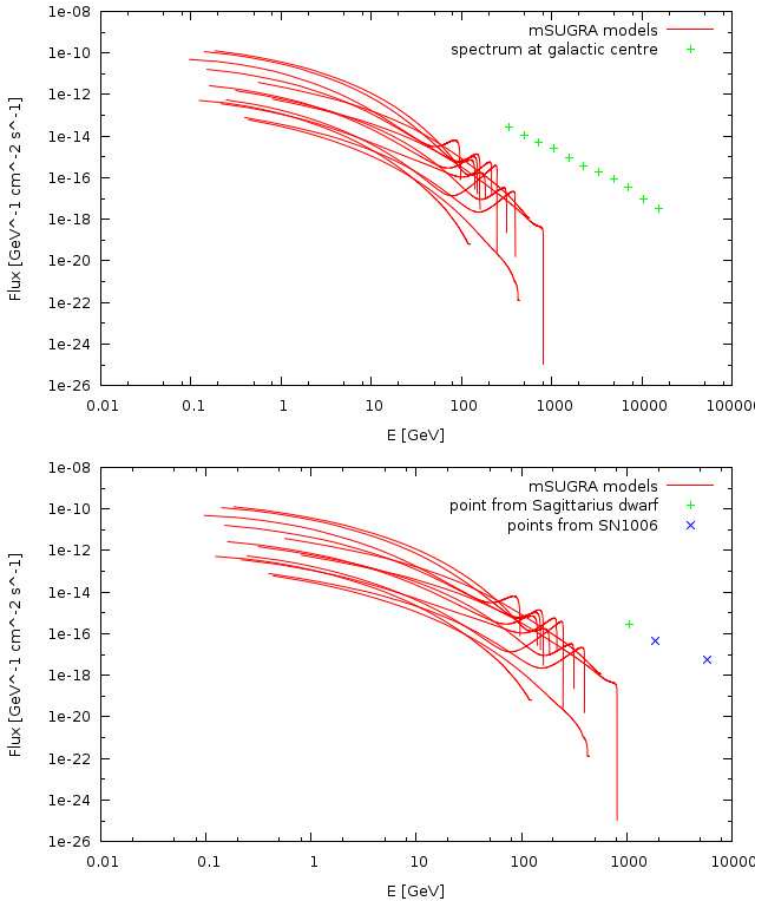

Figure 5.4: On top: The spectrum of the galactic centre from H.E.S.S. with the spectra from the mSUGRA benchmark models. Below: Spectra from other regions are compared to the dark matter spectra.

5.3 Restrictions on the H.E.S.S. data

In the following runs from different regions, not only the galactic centre, are used. Therefore the whole H.E.S.S. data is studied and restrictions are applied on all the H.E.S.S. data. The energy threshold and the effective areas are studied first. The effective detection area of the H.E.S.S. experiment depends, as mentioned before, on the zenith angle. But also on the offset Θ and the energy of the initial γ. An other important aspect is the optical efficiency that decreases on the timescale of years. All these effects have been considered and Monte Carlo simulations were done, which produced lookup tables for 13 zenith angles for the effective areas. For the analysis done in this thesis especially the low energy range of about 1 TeV is important. Hence the energy treshold has to be low (about 100 GeV). The energy threshold is strongly correlated with the effective areas. The effective areas determine the threshold energy. The threshold energy is about the energy value, where the effective areas start. Actually the integral of the effective areas over energy has to be higher than a certain value at the threshold energy. Therefore, to get a low energy threshold, the effective areas need to be well understood in the low energy region. For this reason only runs with zenith angles up to 40° are used, as the effective areas in this region are more in favour of a low energy analysis. A few effective areas for different zenith angles as well as for the different phases of optical efficiency are shown in Fig. 5.5 in the top panel. The blue line is the effective area for a 60° zenith angle, the black line for a 20° and the red line for a 0° zenith angle. It is shown that the energy threshold is much higher for the 60° zenith angle than for the other two. Therefore a cut on the zenith angle is applied and only data with a zenith angle smaller than 40° are used. In addition the behaviour of the effective areas for different optical efficiencies is studied, see Fig. 5.5 in the lower panel. The differences between a higher (Fig. 5.5 lower panel black curve) and a lower (Fig. 5.5 lower panel red curve) optical efficiency are not very large. Therefore all data, independent of the optical efficiency, under which they are taken, are used.
In addition only data, which are taken under good weather conditions and with three or more telescopes are used. Applying all these selection criteria to the list of H.E.S.S. runs about 2000 runs are left. The way they are spread across the sky is shown in Fig. 5.6. The coordinates there are right ascension and declination on the top and galactic coordinates, latitude b and longitude l, on the bottom. In both pictures the galactic plane is visible due to the large amount of runs taken for the galactic survey.

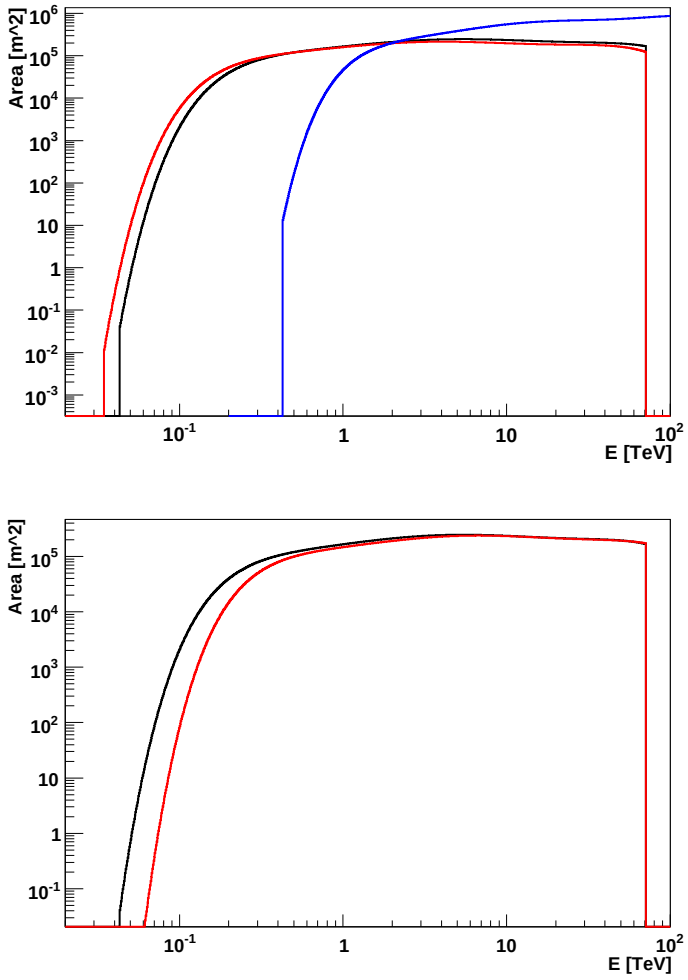

Figure 5.5: On top effective areas from the look up tables under different zenith angles are plotted. Red is 0°, black 20° and blue 60° zenith angle. Below two effective areas for different optical efficiencies are shown. High optical efficiency is black and lower optical efficiency red.

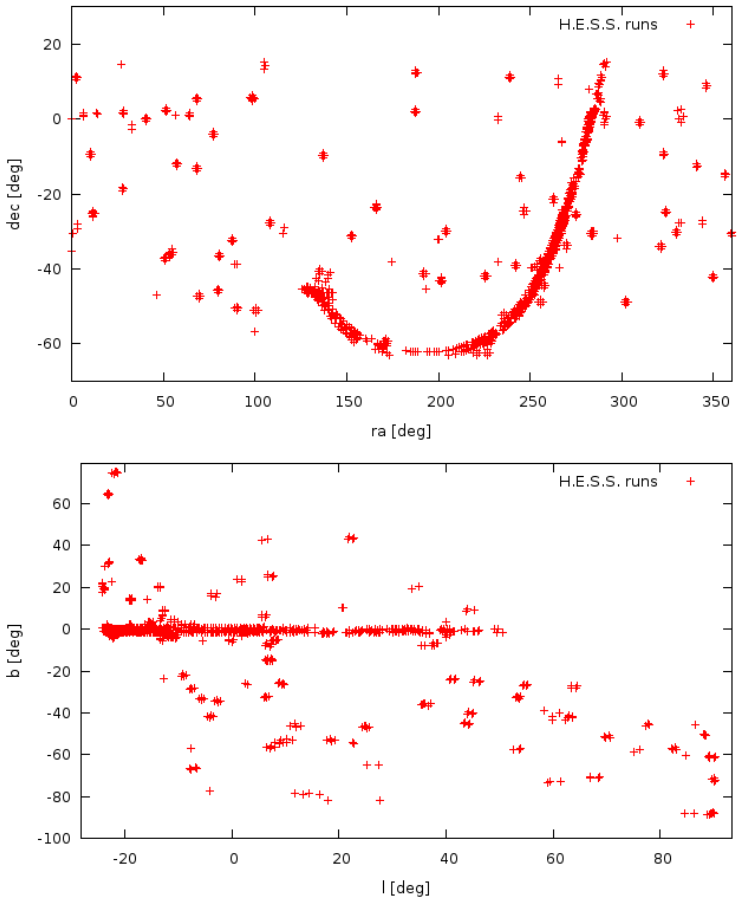

Figure 5.6: The distribution of the H.E.S.S. runs, that passed the selection criteria, is shown. On top in right ascension and declination and below in galactic coordinates.

5.4 Upper limit from measurement of the Sagittarius Dwarf galaxy

The upper limit derived in "Observations of the Sagittarius Dwarf galaxy by the H.E.S.S. experiment and search for a Dark Matter signal"[30] is reproduced. [30] presents the calculation of an upper limit on the velocity weighted annihilation cross section $\langle \sigma v \rangle$ of the dark matter particle. In the following a short summary of the content of the paper is given.
In the introduction of the paper the search for dark matter in the Sagittarius Dwarf galaxy is motivated. It is stated that WIMPs are more likely to detect indirectly if a region with high dark matter density is studied. H.E.S.S. has observed several regions that are likely to fullfill this requirement and the Dwarf Spheroidal galaxies "Sagittarius Dwarf" and "Canis Major" are especially promising. The next section of the paper deals with the description of the H.E.S.S. experiment and the dataset that is used. A total of 25 runs, each 28 minutes long, is used. This sums up to an observation time of about 11 hours. The average zenith angle is about 19°, while the angular offset is about ±0.7°. The analysis of the data is shown. Important there is the chose of $\Theta_{cut} = 0.14°$ according to the assumption of a point like source. Two different density profiles where tested for the Sagittarius Dwarf galaxy, a NFW profile and a cored profile. These profiles were then folded with the H.E.S.S. point spread function. With the information of the $N_{on} = 437$ events, the $N_{off} = 4270$ events and the ratio $\alpha = 10.1$ the 95% confidence level upper limit $N_{\gamma}^{95\%\,C.L.} = 56$ on the number of observed γ-rays is derived. Also a limit $(\Phi_{\gamma}(E_{\gamma} > 250\,GeV) < 3.6 \times 10^{-12}\,cm^{-2}s^{-1}\ (95\%\,C.L.))$ on the γ-ray flux is calculated. The theoretical basis for these calculations is presented in the next section of the paper. There the γ-ray flux from a spherical dark matter halo is given

$$\frac{d\Phi(\Delta\Omega, E_{\gamma})}{dE_{\gamma}} = \frac{1}{4\pi} \frac{\langle \sigma v \rangle}{m_{DM}^2} \frac{dN_{\gamma}}{dE_{\gamma}} \times \bar{J}(\Delta\Omega)\Delta\Omega \tag{5.3}$$

where $J(\Delta\Omega)$ is the integral over the line of sight of the dark matter density ρ^2. (Here the notations are chosen to be the same as in the original paper [30] not to be confused with the notations in the other section of this thesis, where $\bar{J}(\Delta\Omega)\Delta\Omega$ is given as $\langle J^{AP}(\psi) \rangle_{\Delta\Omega}$). Another subsection in this theoretical part is devoted to the derivation of the halo profiles of the Sgr dwarf galaxy. In the next subsection the essential formula, that are used for recalculations are then described. First the number of expected γ-rays is given by:

$$N_{\gamma} = T_{obs} \int_0^{m_{DM}} A_{eff}(E_{\gamma}) \frac{d\Phi(\Delta\Omega, E_{\gamma})}{dE_{\gamma}}\, dE_{\gamma} \tag{5.4}$$

Here $A_{eff}(E_\gamma)$ are the effective areas of the H.E.S.S. telescopes obtained via Monte Carlo simulations. Combining equation 5.4 with the equation of the flux, Eq. 5.3 then yields the 95% C.L. upper limit on the velocity weighted cross section versus the dark matter particle mass, see Eq. 5.5.

$$\langle \sigma v \rangle_{min}^{95\%\,C.L.} = \frac{4\pi}{T_{obs}} \frac{m_{DM}^2}{\bar{J}(\Delta\Omega)\Delta\Omega} \frac{N_\gamma^{95\%\,C.L.}}{\int_0^{m_{DM}} A_{eff}(E_\gamma) \frac{dN_\gamma}{dE_\gamma}\, dE_\gamma} \tag{5.5}$$

In [30] for dN/dE_γ a parametrisation from Bergstroem et al. [31] is chosen. The last sections of the paper then discuss the results obtained with the before explained methods and assumptions.
Now the basic idea is to recreate the plot (see Fig. 5.7) of the paper "Observations of the Sagittarius Dwarf galaxy by the H.E.S.S. experiment and search for a Dark Matter signal," Astropart. Phys. **29**, 55 (2008). To achieve this Eq. 5.5 is used.

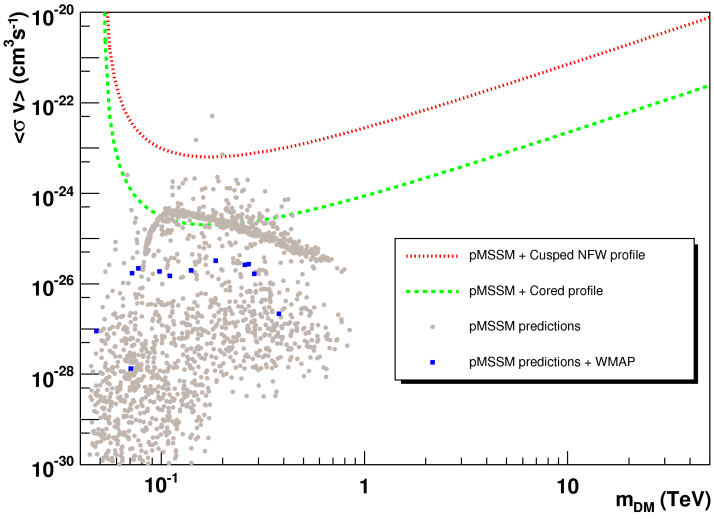

Figure 5.7: The upper limit on σv as shown in [30]. The red curve is chosen for recreating.

The following variables within Eq. 5.5 are considered to be constant and the values are chosen according to the paper:

$$\begin{aligned} T_{obs} &= 11 \cdot 60 \cdot 60\, s \\ \bar{J}(\Delta\Omega)\Delta\Omega &= 2.2 \times 10^{24}\, GeV^2 cm^{-5} \cdot 2 \times 10^{-5}\, sr \\ N_\gamma^{95\%\, C.L.} &= 56 \end{aligned}$$

These values are then, including the factor 4π, combined to a single constant:

$$\frac{4\pi \cdot N_\gamma^{95\%\, C.L.}}{T_{obs} \cdot \bar{J}(\Delta\Omega)\Delta\Omega} \tag{5.6}$$

In order to get from the GeV^2 to TeV^2 this constant factor is multiplied with 10^6. This leaves the following term to be determined:

$$\frac{m_{DM}^2}{\int_0^{m_{DM}} A_{eff}(E_\gamma) \frac{dN_\gamma}{dE_\gamma}\, dE_\gamma} \tag{5.7}$$

The effective areas are taken from the look up tables. The effective areas, which are used, are at 20° zenith angle, 0.5° offset and for the first phase of optical efficiency (0510). The shape of the effective area is shown in Fig. 5.9 on top. There the name is again chosen as described in the section "effective areas". The lookup effective areas are not the same as the effective areas from the actual analysis used in the paper. Nevertheless the difference is neglectable. The parametrisation for the dark matter spectrum dN_γ/dE_γ is taken from the reference Bergstroem et al. [31]. The formula is given in Eq. 5.8.

$$\frac{dN_\gamma}{dE_\gamma} = \frac{0.73}{m_{DM}} \frac{e^{-7.8\frac{E_\gamma}{m_{DM}}}}{\left(\frac{E_\gamma}{m_{DM}}\right)^{3/2}} \tag{5.8}$$

All this filled in Eq. 5.5 then yields the upper limit plotted in Fig. 5.8. Also the upper limit from [30] is indicated by red dots. Compared to the plot of the upper limit given in [30] (see Fig. 5.7 the red curve and Fig.5.8 the red dots) clear differences are visible. Nevertheless the order of magnitude of the limit is the same for both curves. The difference lies mainly in a shift to higher energies for the recreated curve. In order to get rid of this contradiction several parts of the recalculation are searched for errors:

- units have been checked.
- the influence of the optical efficiency. The different optical efficiencies could lead to the different results. So the effective area used is compared to the

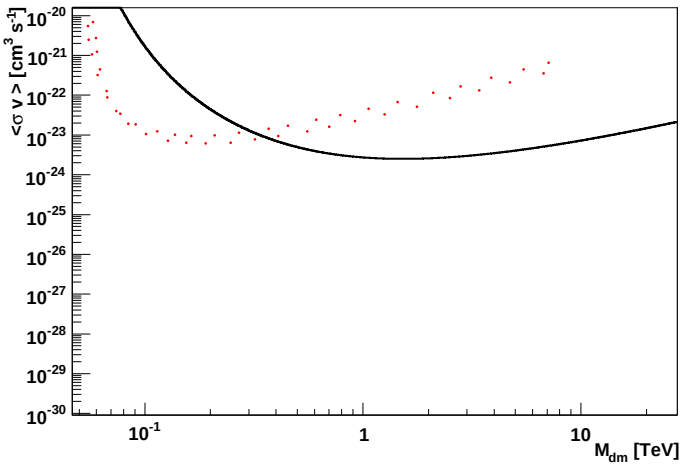

Figure 5.8: Upperlimit on σv derived with the parametrisation from Bergstoem et. al. [31](black). The red point correspond to the upper limit derived in [30].

effective area from the lookups, where the full optical efficiency is assumed. This is shown in Fig.5.9 in the middle, where the two different effective areas are plotted in one histogram. The red one is the one with full optical efficiency and the black one is from phase 1b.

- influence of zenith angle and offset. Also tested is the shape of the effective areas for different offset and different zenith angles, which are all shown in Fig. 5.9 on the bottom.

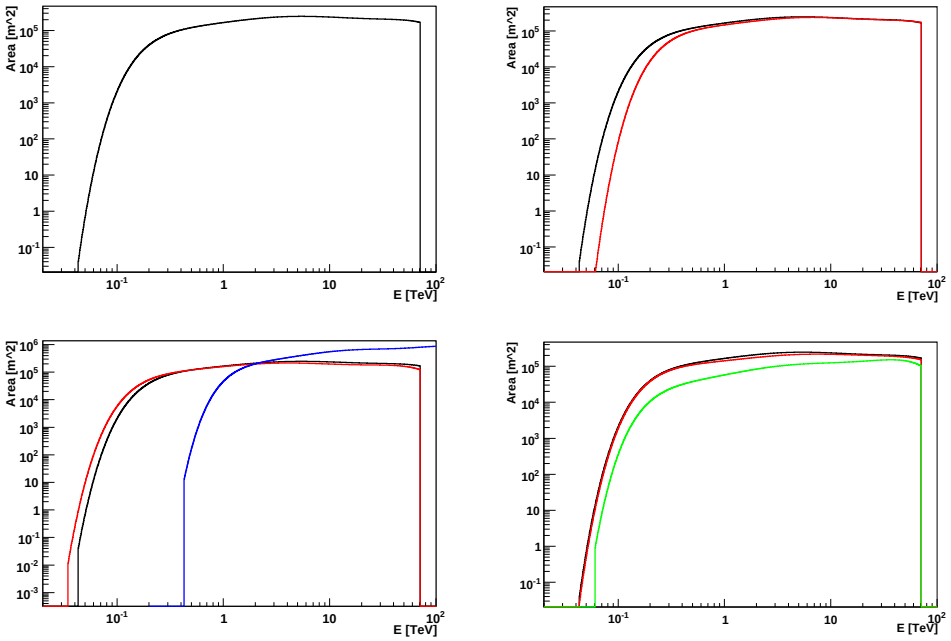

Figure 5.9: On top on the left the effective area from the lookup table, which is used fro the first calculation is shown. There the zenith angle is 20° and the offset 0.5°. The optical efficiency corresponds to phase one. On top on the right a comparison between the effective areas for higher optical efficiency (black) and lower optical efficiency (red) is shown. Below follow three effective areas for three different zenith angles (left). Black resembles the used 20° zenith angle, while red corresponds to 0° and blue to 60° zenith angles. Eventually on the right three effective areas for different offsets are plotted (green is 2.0° offset, red is 1.0° offset and black is 0.5° offset).

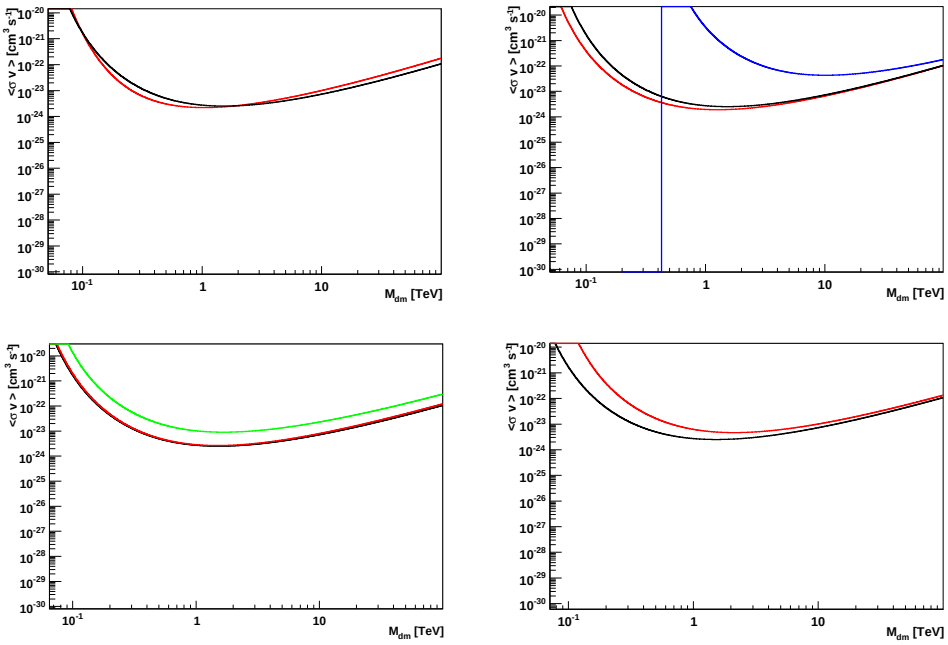

Figure 5.10: Upper limits on σv. On top left the Bergstroem (black) and the Tasitsiomi (red) parametrisation are plotted. On the right the upper limits for three different zenith angles (red 0°, black 20° and blue 60°) and below on the left three different offsets (green is 2.0° offset, red is 1.0° offset and black is 0.5° offset) are given. On the bottom on the right the upper limit for two different optical efficiencies is shown. The red curve has lower efficiency than the black curve.

As there is a difference for the optical efficiencies also the two resulting upper limits are plotted for comparison into one histogram, see Fig. 5.10 the third panel. Indeed a shift to lower energies is visible there, but it is not nearly big enough to explain the difference to the upper limit given in [30]. During further investigations it turned out that in [30] a different parametrisation was used. The parametrisation used there was from Tasitsiomi et al. [32]. So the parametrisation (given in Eq. 5.9) is derived from formula 6 and 7 from [32]. The same calculations as before are then done with this parametrisation for dN_γ/dE_γ.

$$\frac{5}{8}\frac{1}{m_{DM}}\left(\frac{16}{3}+\frac{2}{3}\cdot\left(\frac{E_\gamma}{m_{DM}}\right)^{-1.5}-4\cdot\left(\frac{E_\gamma}{m_{DM}}\right)^{-0.5}-2\cdot\left(\frac{E_\gamma}{m_{DM}}\right)^{0.5}\right) \tag{5.9}$$

The same effective area as for the first calculation is used. This then results in the upper limit shown in Fig. 5.10 on top (the red curve). In Fig. 5.10 also the upper

limit gained with the Bergstroem parametrisation is shown. Both parametrisations look almost the same. Hence again no agreement with the upper limit derived in [30] is achieved. This result is not very comforting. Therefore in order to show that the recalculation of the limit is correct, it is compared with a more recent study on the same source [2]. The upper limit from [2] only differs from the upper limit of [30] in the number of $N_{\gamma}^{95\%\,C.L.}$. The number is 82 instead of 56. With this included and with the Bergstroem parametrisation [31] used, the black curve in Fig. 5.11 is created. The pink points in Fig. 5.11 are the upper limit from the recent study [2]. The disagreement between the black curve and the pink points is much smaller than the difference with the upper limit from [30]. In addition this small difference can easily be explained with the usage of different effective areas. In conclusion the upper limit seems to be recalculated correct, but the disagreement with the original [30] still needs to be explained. Contact with the corresponding author of the paper has been made and the problem will be solved in cooperation with him.

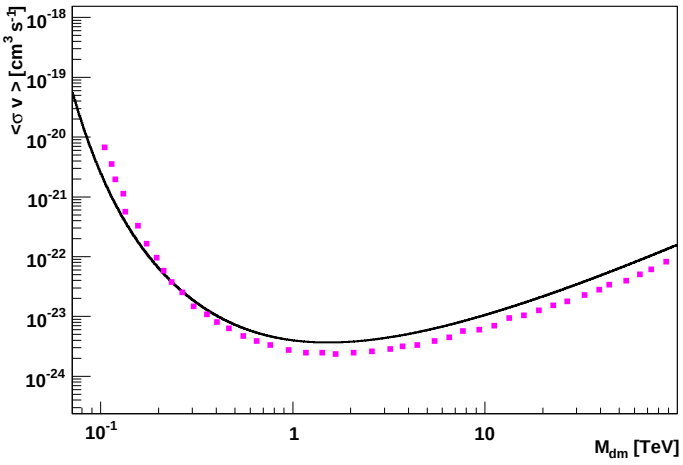

Figure 5.11: The upper limit derived with the Bergstroem parametrisation and the upper limit from the recent study (pink dots) [2].

5.5 Observation time dependence

Whenever trying to detect a very weak source, like a dark matter source, the observation time on the source position is essential. The longer a source is studied the higher is the possibility for its detection. Therefore here the number of expected gamma-rays from dark matter annihilation and their dependence on the observation time is shown. Also the direction, in which the dark matter source is assumed is important hence several directions are studied. The number of expected gamma-rays is calculated as described in [30], see also Eq. 5.4. This is done for a large number of pMSSM models. The parameters for these models are derived in a scan done with DarkSUSY by Andreas Spies. The numbers of expected gamma-rays are then given depending on the neutralino mass for different observation times. The region chosen is the galactic centre, because the number of gamma-rays is expected to be highest there due to the dark matter density profile. For these calculations then the observation time needed for a five sigma detection of a dark matter source can be determined. This is done under the assumption that there are no background or other sources in the tested region. In Fig. 5.12 the expected number of gamma-rays for different observation times is shown for different pMSSM models. The pMSSM models are gained in a scan over the parameter space done with DarkSUSY by Andreas Spies. In Fig. 5.12 the expected number of gamma-rays from supersymmetric dark matter annihilation at the galactic centre for one H.E.S.S. run is shown. An effective area from the look up table is used. In Addition the expectations for longer observation times have also been plotted, see Fig. 5.12 in the lower panel. In order to calculate the number of γ-rays needed for a five sigma signal the following formula (after Li and Ma [26]) is used:

$$S = \frac{N_{on} - \alpha N_{off}}{\sqrt{N_{on} + \alpha^2 N_{off}}} \,. \tag{5.10}$$

S is the significance, while N_{on} is the number of on events and N_{off} is the number of off events. α corrects different acceptances in the On and the Off region and different observation times. Now for the very simple assumption of no background ($N_{off} = 0$) the number of events N_{on} is

$$N_{on} = S^2 \tag{5.11}$$

and for a significance $S = 5$ results $N_{on} = 25$. In Fig. 5.13 a violet dashed line is plotted at $N_{on} = N_{exp} = 25$. The expected number of gamma-rays for pMSSM models is filled in for the same observation times as before. It can be seen that for observation times of about 100 hours and in a situation with no background most models could be excluded. But unfortunately there is a lot of background at the galactic centre.

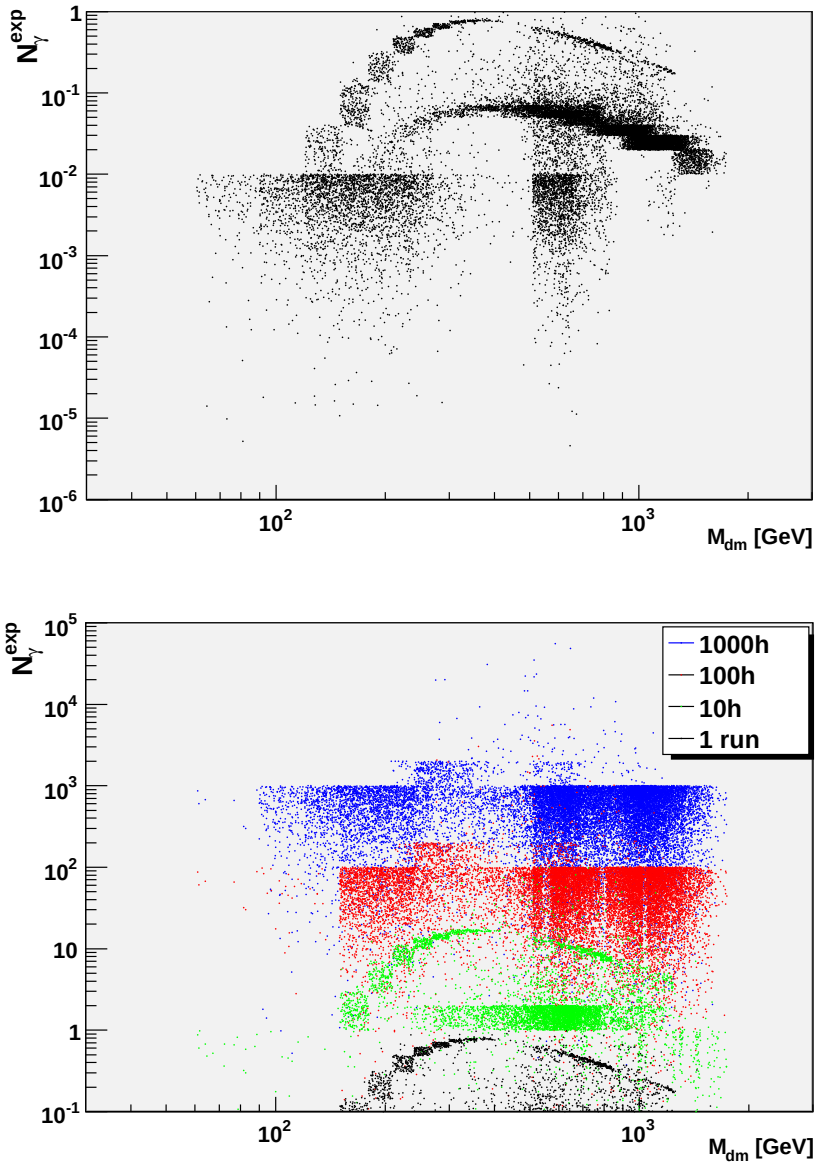

Figure 5.12: Expected number of gamma-rays from dark matter annihilation for different observation times. Every entry corresponds to one pMSSM model. On top the observation time is one run (28 minutes). Below different observationtimes are given (1 run, 10 hours, 100 hours and 1000 hours).

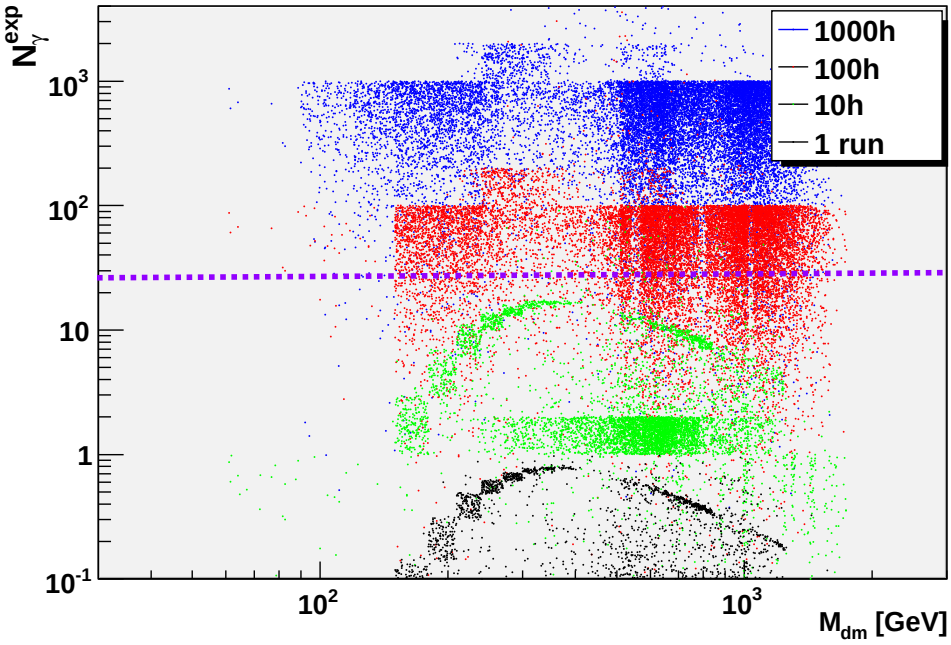

Figure 5.13: The expected number of gamma-rays for different observation times. A violet dashed line is plotted, where at five sigma limit of 25 events.

5.6 New Method

All the spectra measured by H.E.S.S. go up to more than 10 TeV. But the spectrum from the annihilation of a supersymmetric dark matter only goes up to the neutralino mass, which is not higher than a few TeV. Hence a comparison between a spectrum measured by H.E.S.S. and a spectrum from dark matter annihilation is not possible. Upperlimits though, as described in the section before, can at least exclude certain regions of the parameter space. But still these limits are not very constraining. Hence an other way to search for dark matter is suggested and described in the following.
The density distribution of dark matter in the milky way is studied again. Different density profiles are visible in Fig. 5.14. The profiles are plotted in arbitrary units, because only the ratio between the values at the galactic centre and away from the centre are important. All the profiles are spherically symmetric. This is nicely seen in Fig. 5.14. The relation between the galactic latitude b and the galactic longitude l and the angle ψ of the direction of the dark matter source is the following:

$$\psi = \sqrt{b^2 + l^2} \tag{5.12}$$

In Fig. 5.14 as mentioned before the peak of the density at the galactic centre is seen. It is explained above, that because of this a higher γ-ray flux is expected from the galactic centre than from other regions.

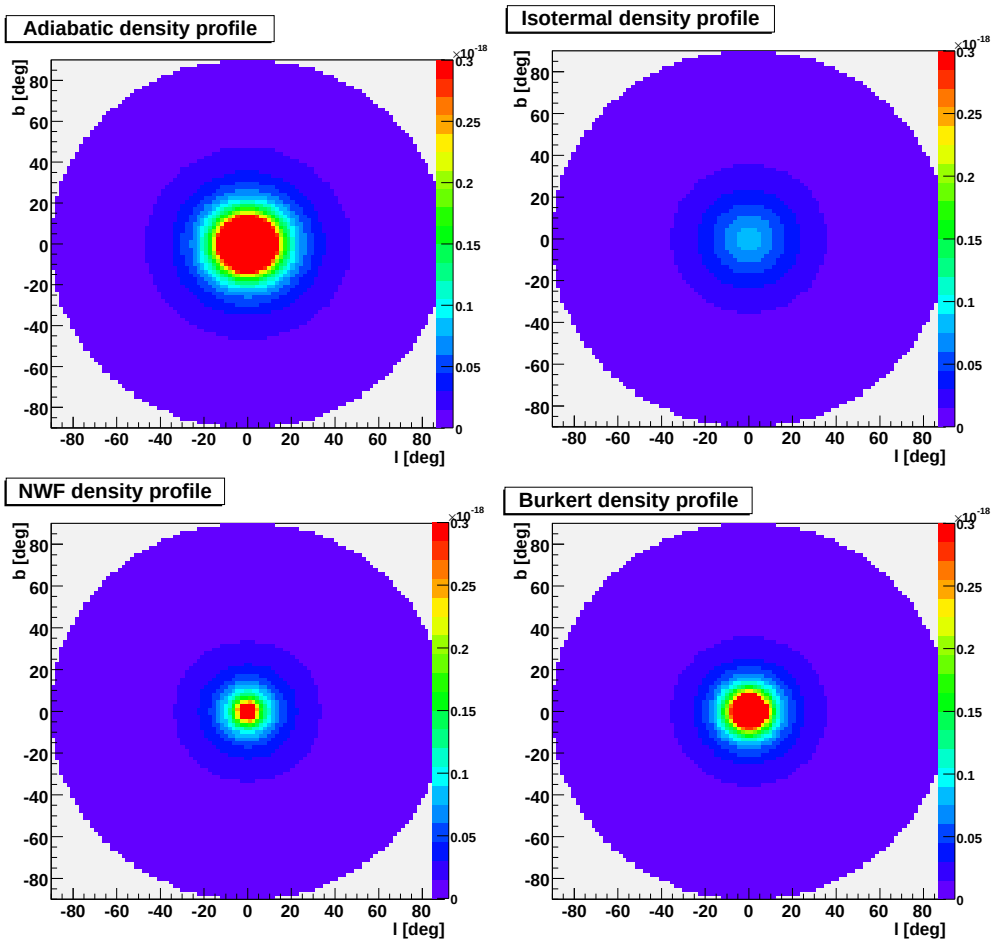

Figure 5.14: Different dark matter density profiles. All show a maximal density at the galactic centre.

For the following only the NFW profile is used. This is done, because there the density and therefore the flux of γ-rays falls of by about a factor of ten to the regions away from the galactic centre. The idea is now to take data from runs at the galactic centre and off the galactic centre and compare the fluxes. The assumption, that goes in here, is that the background of γ-rays is the same at the galactic centre and outside. This is a very simple assumption, but if it is true the difference of the amount of γ-rays from dark matter would be visible in the flux. Different gamma-ray fluxes for one mSUGRA model are drawn in Fig. 5.15. The flux at the galactic centre ($\psi = 0.5°$, red) and away from the galactic centre (corresponding to an angle ψ of about 22°, green) is given. The difference between the two curves is almost the same as red curve.

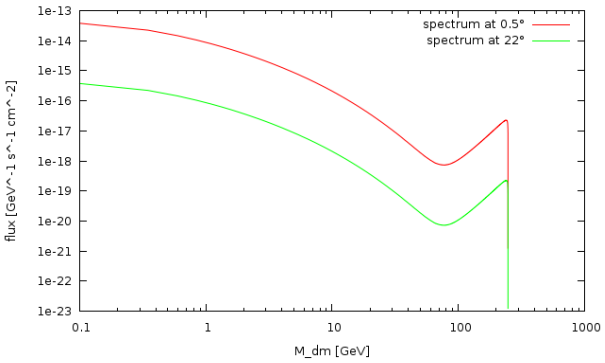

Figure 5.15: Gamma-ray flux from supersymmetric dark matter annihilation at the galactic centre (red) and at about 22° away from it (green) are given.

The H.E.S.S. runs, that are selected before (see section 5.2), are plotted over the NFW dark matter density profile, see Fig. 5.16. A lot of possible regions for the analysis exist. When chosen region to compare certain things have to be taken into account. First the zenith angles of the observations are not allowed to differ to much. The effective areas are different for different zenith angles and also other systematics might be. Therefore a range of 10° is chosen in the zenith angles of the different regions. In addition the optical efficiency should be the same for the observations. In conclusion similar observation conditions are needed for the regions. In the following an example analysis for two regions, namely the galactic centre and SN1006, is presented. SN1006 is a very faint source, that only was discovered recently. The coordinates of SN1006 are about 225.75° right ascention (r.a.) and -41.5° declination (dec.) [33]. The galactic centre has the coordinates about 266.25° right ascension and -28° declination [25]. Now for the analysis the test positions are shifted 2° off the sources. So the test coordinates are 264.5° r.a. and -26.5° dec. for the galactic centre and 223.7° r.a. and -39.5° dec. for SN1006. This

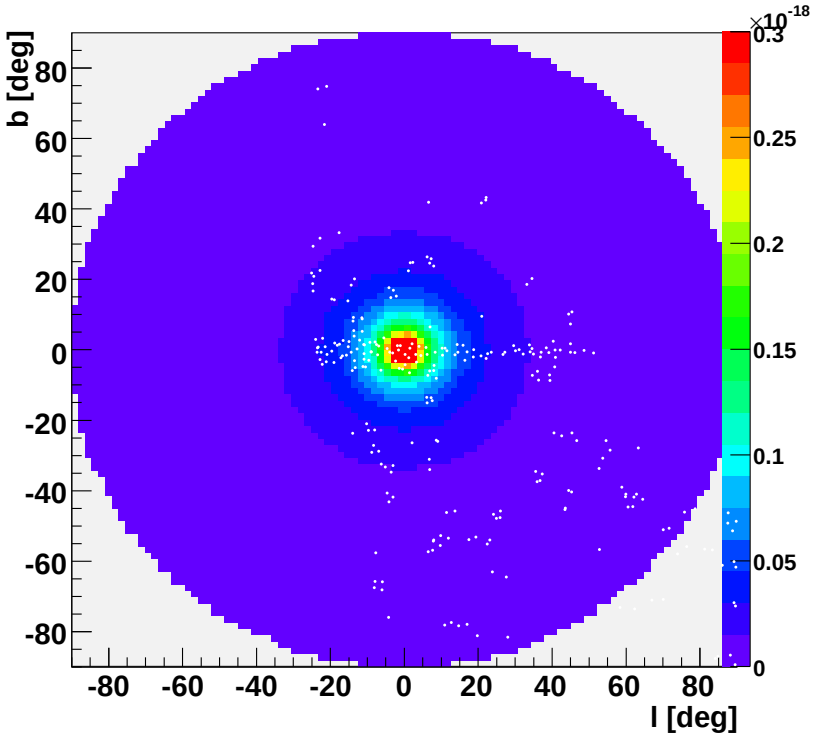

Figure 5.16: NFW dark matter density profile with the distribution of H.E.S.S. runs (withe squares).

is done to reduce the influence of the known gamma-ray sources, which effect the background. For the test 27 runs from the galactic centre and 79 runs from SN1006 are chosen. The runs have been taken under an average zenith angle of about 20° and about the same optical efficiency. For the analysis of the two sources the ringbackground and std cuts are used. The on flux of the two spectra is subtracted from one another. The result is given in Fig. 5.17. The difference of the two fluxes is positive. This is nice, since it might hint to dark matter. Nevertheless the points are not constant and they go up to energies as high as 8 TeV. Also the uncertainties on this analysis are too large to claim anything. The errors on the difference are not given here, but they are very large. In addition the assumption about the background being the same in the compared regions might not be true. Furthermore the analysis contains systematics, that are not yet understood. Especially in the low energy range.

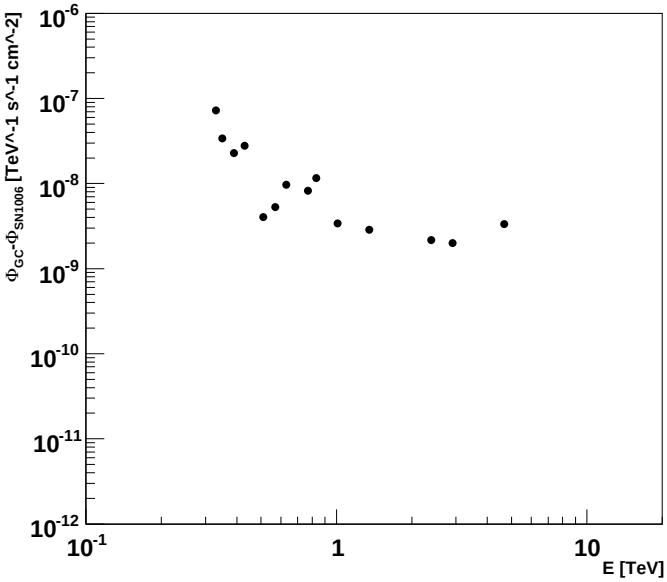

Figure 5.17: The result from the analysis. The flux from SN1006 (Φ_{SN1006}) is subtracted from the flux from the galactic centre (Φ_{GC}).

6 Conclusion and Outlook

During the work on this thesis an overview over the subject of dark matter and the searching for it with an IACT has been achieved. The different topics, which are covered, present all the basics needed for further investigations. In conclusion the following has been done:

A basic understanding for supersymmetric dark matter and its properties is achieved. The programme DarkSUSY, which is a very important tool to calculate supersymmetric dark matter properties, is used. Variables have been recalculated and a satisfying agreemet with DarkSUSY is achieved.

An upper limit is recalculated. Some differences appear with the original. The upper limit could not be reproduced, but the calculated limit agrees well with a more recent study. Work is still in progress to find the cause of the differences.

Further a study on the expected number of gamma-rays from the annihilation of supersymmetric dark matter is made. The very simple assumption of no background leads to a rough estimate of observation time needed to exclude a dark matter source. In future studies this calculation can be expanded to situations with different backgrounds. Then a more precise estimate of the observation time necessary to actually detect dark matter can be given.

Eventually a new searching method is introduced. The method is tested for an example set of two regions and the results are shown. Further tests are necessary in order to draw significant conclusions. A lot of ideas exist how to improve the new method. Work can be done in the reduction and understanding of systematic effects in the analysis, especially in case of the effective areas. Furthermore other regions can be compared to the galactic centre, which might reveal the shape of the dark matter halo. It is possible to even combine more regions with the same predicted dark matter density to get better statistics and to eliminate more of the background fluctuations.

7 Appendix

7.1 DarkSUSY5.0.1

DarkSUSY5.0.1 is a recent version of the DarkSUSY programme package, that became available to the public in August 2008. The program is a numerical package to calculate the properties of supersymmetric dark matter. It includes calculations of the relic density and also takes into account recent accelerator constraints. Neutrino and gamma-ray fluxes from the annihilation of supersymmetric dark matter can be determined with it.

The DarkSUSY package can be used separately but has also interfaces with other programmes. These other programmes are used to calculate the mass spectrum of different supersymmetric models. A very simple MSSM model with only seven parameters is offered in DarkSUSY. Furthermore an interface to ISASUGRA (see [34]) exists, which makes it possible to calculate mSUGRA models. Therefore the parameters of mSUGRA at the GUT scale are entered. ISASUGRA then calculates the mass spectrum of the particles at the electroweakscale. These parameters at the electroweaksclae are then used by DarkSUSY. In addition an interface to SUSPECT (for details see [35]) was written by Andreas Spies. SUSPECT calculates mass spectra at the electroweakscale up to second loop processes (or at least most important second loop terms are taken into account). In SUSPECT not only parameters of mSUGRA can be entered but also parameters for the pMSSM model. The results are again used by DarkSUSY.

Bibliography

[1] F. Aharonian *et al.* HESS observations of the galactic center region and their possible dark matter interpretation. Phys. Rev. Lett. **97**, 221102 (2006) [Erratum-ibid. **97**, 249901 (2006)]

[2] C. Farnier et al. Search for dark matter annihilation signals from dwarf spheroidal galaxies with H.E.S.S. . *Proceedings of the IDM 2008, Stockholm.*

[3] P. Gondolo, J. Edsjo, P. Ullio, L. Bergstrom, M. Schelke, E.A. Baltz, T. Bringmann and G. Duda, http://www.physto.se/ edsjo/darksusy

[4] Clifford M. Will. The Confrontation between General Relativity and Experiment. Living Rev. Relativity 9, (2006), 3. URL (cited on 22.10.2008): http://www.livingreviews.org/lrr-2006-3

[5] A. Einstein. On the General Theory of Relativity. Sitzungsber. Preuss. Akad. Wiss. Berlin (Math. Phys.) **1915**, 778 (1915) [Addendum-ibid. **1915**, 799 (1915)].

[6] Website: http://map.gsfc.nasa.gov/

[7] T. Wyatt. High-Energy Colliders And The Rise Of The Standard Model. Nature **448**, 274 (2007).

[8] M. Kowalski *et al.* Improved Cosmological Constraints from New, Old and Combined Supernova Datasets.

[9] F. Zwicky. On the Masses of Nebulae and of Clusters of Nebulae. Astrophys. J. **86**, 217 (1937).

[10] J. J. Mohr, B. Mathiesen and A. E. Evrard. Properties of the Intracluster Medium in an Ensemble of Nearby Galaxy Clusters. Astrophys. J. **517**, 627 (1999)

[11] S. Dye and S. Warren. Constraints on dark and visible mass in galaxies from strong gravitational lensing.

[12] Y. Ashie *et al.* Evidence for an oscillatory signature in atmospheric neutrino oscillation. Phys. Rev. Lett. **93**, 101801 (2004)

[13] S. P. Martin. A supersymmetry primer.

[14] M.E. Peskin and D.V. Schroeder. *An Introduction to Quantum Field Theory, P. 700 f.*. Westview Press, 1995.

[15] P. Gondolo, J. Edsjo, P. Ullio, L. Bergstrom, M. Schelke and E. A. Baltz. DarkSUSY: Computing supersymmetric dark matter properties numerically. JCAP **0407**, 008 (2004)

[16] V. I. Tretyak and Yu. G. Zdesenko. New limit on the proton lifetime from neutrino experiments with heavy water. Phys. Atom. Nucl. **66**, 514 (2003) [Yad. Fiz. **66**, 541 (2003)].

[17] R. Wanke. Precision Standard Model Tests with Kaons.

[18] R. L. Arnowitt and P. Nath. Supersymmetry and supergravity: Phenomenology and grand unification.

[19] D. I. Kazakov. Beyond the standard model (in search of supersymmetry).

[20] F. D. A. Hartwick. A Model for Dark Matter Halos.

[21] J. F. Navarro, C. S. Frenk and S. D. M. White. A Universal Density Profile from Hierarchical Clustering. Astrophys. J. **490**, 493 (1997)

[22] V. Berezinsky, V. Dokuchaev and Y. Eroshenko. Small-scale clumps in the galactic halo and dark matter annihilation. Phys. Rev. D **68**, 103003 (2003)

[23] T. Bringmann, L. Bergstrom and J. Edsjo. New Gamma-Ray Contributions to Supersymmetric Dark Matter Annihilation. JHEP **0801**, 049 (2008)

[24] Website: http://jelley.wustl.edu/Pages/whipple.html

[25] Homepage of the H.E.S.S. Experiment: http://www.mpi-hd.mpg.de/hfm/HESS/HESS.html

[26] T. P. Li and Y. Q. Ma. Analysis methods for results in gamma-ray astronomy. Astrophys. J. **272**, 317 (1983).

[27] J. Hinton, D. Berge and S. Funk. Background Modeling In Ground Based Cherenkov Astronomy. *Prepared for 7th Workshop on Towards a Network of Atmospheric Cherenkov Detectors 2005, Palaiseau, France, 27-29 Apr 2005*

[28] F. Aharonian *et al.* Observations of the Crab nebula with HESS. Astron. Astrophys. **457**, 899 (2006)

[29] A. M. Hillas. Cherenkov light images of eas produced by primary gamma. *Proceedings of the 19th ICRC, La Jolla, 3:445, 1985.*

[30] F. Aharonian *et al.* Observations of the Sagittarius Dwarf galaxy by the H.E.S.S. experiment and search for a Dark Matter signal. Astropart. Phys. **29**, 55 (2008)

[31] L. Bergstrom, P. Ullio and J. H. Buckley. Observability of gamma rays from dark matter neutralino annihilations in the Milky Way halo. Astropart. Phys. **9**, 137 (1998)

[32] A. Tasitsiomi, J. M. Siegal-Gaskins and A. V. Olinto. Gamma-ray and synchrotron emission from neutralino annihilation in the Large Magellanic Cloud. Astropart. Phys. **21**, 637 (2004)

[33] M. Naumann-Godó et al. Discovery of SN 1006 in VHE Gamma-Rays by H.E.S.S. . *Proceedings of the Gamma 08 Symposium, Heidelberg.*

[34] Website: http://www.phys.ufl.edu/ jblender/isajet/isajet.html

[35] A. Djouadi, J. L. Kneur and G. Moultaka. SuSpect: A Fortran code for the supersymmetric and Higgs particle spectrum in the MSSM. Comput. Phys. Commun. **176**, 426 (2007)

Danksagung

An dieser Stelle möchte ich mich bei all denjenigen bedanken, die mich bei der Anfertigung dieser Diplomarbeit unterstützt haben.

Mein ganz besonderer Dank gilt Prof. Gisela Anton und Prof. Christian Stegmann, die mir diese lehrstuhlübergreifende Diplomarbeit ermöglicht haben.

Für ihre große Hilfsbereitschaft und ihr Engagement möchte ich mich außerdem bei Dr. Ira Jung bedanken. Des Weiteren danke ich Holger Motz für die jederzeitige Beantwortung meiner Fragen.

Erklärung

Hiermit bestätige ich, dass ich diese Arbeit selbstständig und nur unter Verwendung der angegebenen Hilfsmittel angefertigt habe.

Erlangen,

Constanze Jahn